Received: 31 August 2021 | Revised: 10 November 2021 | Accepted: 17 November 2021

DOI: 10.1002/esp.5294

RESEARCH ARTICLE

ESPL WILEY

Surface slip variability on strike-slip faults

Nadine G. Reitman[1,2] | Karl J. Mueller[1] | Gregory E. Tucker[1,3]

[1]Department of Geological Sciences, University of Colorado Boulder, Boulder, CO, USA

[2]Now At: Geologic Hazards Science Center, U. S. Geological Survey, Golden, CO, USA

[3]Cooperative Institute for Research in Environmental Sciences (CIRES), University of Colorado Boulder, Boulder, CO, USA

Correspondence
Nadine G. Reitman, Department of Geological Sciences, University of Colorado Boulder, Boulder, CO 80309, USA
Email: nreitman@usgs.gov

Funding information
National Science Foundation, Grant/Award Number: DGE-1650115

Abstract

Slip in strike-slip earthquakes is spatially variable along a fault, but the degree to which variability over short length scales is inherent to the rupture process or introduced by interpretation and measurement has not been quantified. In this study, we examine the effects of interpretation error on apparent short-wavelength variability in surface slip distributions by comparing numerical landscape evolution models and recent ruptures on strike-slip faults measured by hand and with image correlation. Surface slip distributions measured by hand from 63 strike-slip earthquakes have average spatial variability ($CV_{slip\text{-}spatial}$ = standard deviation/mean) of 0.43–0.52, and a total range of 0.14–1.14. Displacement measurements of offset geomorphic markers from numerical models that simulate constant slip along a fault have average spatial variability of ~0.25–0.40 when measured by hand and no spatial variability when measured by image correlation. Slip distributions from seven recent ruptures measured by image correlation have short-wavelength variability of 0.09–0.29, which is considered inherent to how rupture propagates to the surface. Our results demonstrate that variability innate to the rupture process and introduced by interpretation both contribute substantially to the observed variability in slip distributions measured by hand. Resolving the extent to which short-wavelength variability is inherent to rupture propagation through near-surface material versus an artifact of interpretation furthers understanding of the relationship between surface rupture and fault mechanics and informs interpretation of slip distribution and slip-per-event in past earthquakes.

KEYWORDS
image correlation, landscape evolution model, offset measurement, slip distribution, slip variability, strike-slip fault

1 | INTRODUCTION

As a first approximation, co-seismic slip along a fault follows an elliptical distribution (e.g. Okada, 1985), but in reality, surface slip in strike-slip earthquakes is spatially variable on both short and long wavelengths (Figure 1) (Barka, 1996; Berberian et al., 1984; Choi et al., 2018; Clark, 1972; DuRoss et al., 2020; Fletcher et al., 2014; Gold et al., 2013, 2015; Haeussler et al., 2004a; McGill & Rubin, 1999; Quigley et al., 2012; Rockwell & Klinger, 2013; Rockwell et al., 2002; Shirahama et al., 2016; Sieh et al., 1993; Treiman et al., 2002). The cause of long-wavelength (>1 km) variability is often related to fault structure and geometry, such as multiple fault strands or fault step-overs (e.g. Manighetti et al., 2015b; Wesnousky, 2008), but there are several potential causes of short-wavelength (<1 km) variability, and it is not yet clear which are the main contributors. Short-wavelength spatial variability in surface slip may be due to natural variation inherent to the rupture process (inherent variability), introduced by incomplete or inaccurate measurement of tectonic slip (introduced variability), or a combination of both (e.g. Gold et al., 2013; McGill & Rubin, 1999; Rockwell et al., 2002). Quantifying the amount and relative contributions of inherent and introduced variability will inform fault displacement hazard analysis (e.g. Petersen et al., 2011) and interpretation of past earthquake ruptures.

Inherent spatial variability over short wavelengths may be caused by multiple characteristics of the fault zone and rupture process. Rock mechanics experiments give a theoretical upper limit on the elastic strain limit in rocks of 0.5%, above which permanent deformation (i.e. inelastic strain) occurs. This limit implies that slip variability

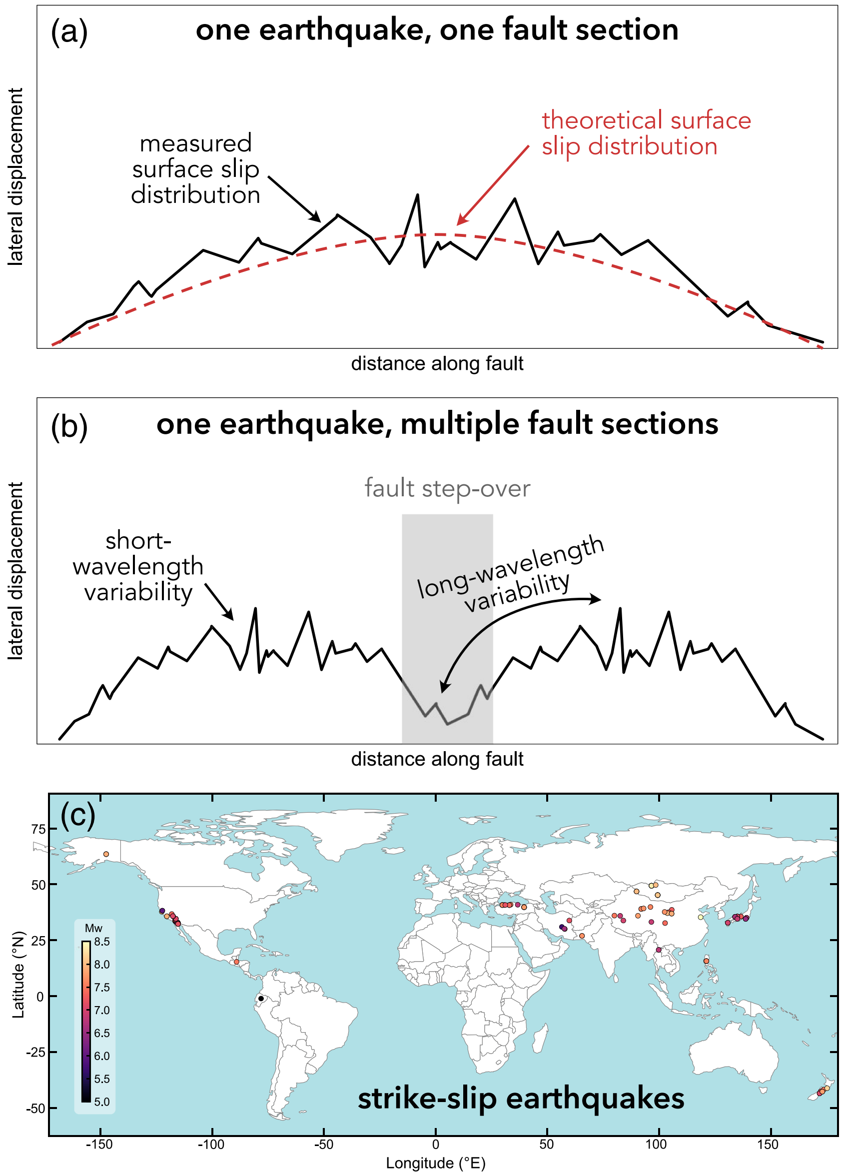

FIGURE 1 Conceptual surface slip distributions for a single earthquake rupturing (a) one or (b) multiple fault sections. These illustrate the short- and long-wavelength variability typical of slip distributions measured from recent strike-slip surface ruptures. (c) Map of earthquakes included in this study [Color figure can be viewed at wileyonlinelibrary.com]

greater than 0.5 m over a lateral span of 100 m should be due to introduced sources; however, exceedance of the elastic strain limit has been observed in many recent surface ruptures (Barnhart et al., 2020b; Brooks et al., 2017; Cheng & Barnhart, 2021; Scott et al., 2019). Permanent deformation is therefore common and may be a large source of short-wavelength variability. Other potential sources of inherent short-wavelength variability include fault roughness (e.g. Bruhat et al., 2019; Milliner et al., 2015), rupture velocity (e.g. Robinson et al., 2006), variable slip in past earthquakes (e.g. Emre et al., 2020; McGill & Rubin, 1999), fault geometry (e.g. Bruhat et al., 2019; Milliner et al., 2016b), and the strength of near-surface material (e.g. Ma & Andrews, 2010; Zinke et al., 2014). Distributed deformation, which may be caused by a combination of these factors, occurs to varying degrees in most surface ruptures and may also contribute to measured slip variability.

Introduced spatial variability from interpretation and measurement of geomorphic markers may contribute additional apparent slip variability. Interpretation and measurement are distinct processes with separate errors. Interpretation is the process of choosing an offset feature or region and reconstructing its pre-earthquake geometry, which involves identifying an offset, identifying the local fault strike, and interpreting the surrounding geomorphology. Measurement is quantifying the offset amount after the preferred and permissible reconstructions have been identified. For modern and paleoseismic earthquakes, offset geomorphic and anthropogenic markers are commonly identified and measured by geologists in the field, on high-resolution optical imagery, and/or on high-resolution digital topography. For modern earthquakes, surface slip is also measured from subpixel correlation of optical images or digital topography acquired before and after an earthquake. Image correlation enables characterizing surface deformation that may be difficult or impossible to measure in the field, such as distributed deformation. For historical earthquakes, however, measuring by hand is the only way to determine the surface slip distribution because there is no record of the landscape prior to the earthquake. Observations of surface slip variability from modern earthquakes thus inform interpretation of surface slip in older earthquakes.

Inherent and introduced variability both likely contribute to the observed spatial variability in surface slip distributions, but their relative contributions remain unknown. The aims of this study are twofold. First, we explore the relationship between spatial variability in slip and earthquake characteristics by compiling surface slip distributions measured by hand from 63 recent, historical, and prehistoric strike-slip earthquakes and analysing the relationship between slip variability and tectonic characteristics. Second, we constrain the relative contributions of inherent and introduced sources of variability by comparing slip distributions measured by hand and with image correlation from recent ruptures and landscape evolution models. Together, these datasets suggest that variability introduced by interpretation and inherent to the rupture process may contribute equally to the observed variability in surface slip distributions measured by hand, and slip distributions of prior ruptures interpreted from geomorphology underestimate total surface slip.

2 | DATA AND METHODS

2.1 | Slip distribution data compilation

We compiled and analysed surface slip distributions from 63 continental strike-slip earthquakes with offsets measured by hand (Figure 1c, Table 1) and seven earthquakes with surface slip measured by image correlation (Table 2; Gold et al., 2015, 2021; Milliner et al., 2016a; Scott et al., 2019; Zinke et al., 2019). This dataset updates published compilations (Baize et al., 2019; Lin et al., 2020; Wesnousky, 2008). We compiled offset measurements from the original sources except for six earthquakes for which we could not access the original data. For these earthquakes, we used data from two of the three prior compilations.

We compare spatial variability of surface slip distributions by calculating a $CV_{slip\text{-}spatial}$ value from the coefficient of variation of all offset measurements along a fault or fault section:

$$CV_{slip-spatial} = \frac{\sigma}{\mu} \quad (1)$$

where σ is the standard deviation and μ is the mean of the offset measurements. We calculate $CV_{slip\text{-}spatial}$ in three ways. For the first method, we use the mean of all measurements greater than zero ('simple mean'). For the second method, we use the mean offset value reported by the authors of the study ('reported mean'). For the fault sections where the authors do not report an average slip value (~15% of datapoints; Table 1), we use the simple mean. For the third method, we use the mean from an interpolated slip distribution based on the observed offset measurements and sampled at regular intervals to avoid spatial bias in locations of offset measurements ('interpolated mean') (e.g. Wells & Coppersmith, 1994). This method could not be applied to all datasets due to a lack of location data. The standard deviation for the first two methods is the standard deviation of all measurements, and for the third method it is the standard deviation of the interpolated slip distribution. None of these methods for calculating mean slip filter out long-wavelength variability.

We use the $CV_{slip\text{-}spatial}$ values calculated from the reported-mean method for the remainder of the analysis. We chose the reported-mean method for three reasons, based on comparing fault sections where we were able to calculate spatial variability with all three methods (Figure 2). First, the reported mean offset may have less spatial bias and be less impacted by long-wavelength variability than the simple mean because most authors account for the distribution of offset measurements in calculating mean slip (e.g. DuRoss et al., 2020). Second, although mean slip is slightly higher for the reported-mean method than for the simple and interpolated methods, and spatial variability is slightly lower, none of these datasets are significantly different at the 95% confidence level (Figure 2a; *t*-test, $p = 0.73$ simple-interpolated; 0.24 simple-reported; 0.10 interpolated-reported). The slight differences in mean values from the three methods cause slight differences in spatial variability, with the reported-mean method having the lowest spatial variability because it has the largest mean (Figure 2b). Third, the interpolated-mean method was not possible for all datasets. In summary, since the mean values calculated from the different methods are not significantly different at the 95% confidence level and the reported mean should have less spatial bias than the simple mean, we use the reported-mean method in reporting $CV_{slip\text{-}spatial}$ values.

We use lateral offset data mapped in the field or on LiDAR or imagery for the most recent earthquake on each fault. For each fault system, we calculate spatial variability based on all offset measurements along the fault and for each fault section, as defined by the authors of the study. We also note which slip distributions are subset from a dataset that includes larger offset measurements that represent multiple earthquakes. We report statistics for the following groups of slip distributions from single earthquakes (Figure 3): (a) all slip distributions from one earthquake ('all data'); (b) single fault sections ('single section'); (c) multiple fault sections ('multiple sections'); (d) slip distributions interpreted from of a dataset that includes larger offsets formed in multiple surface ruptures ('subset'); and (e) slip distributions known to be from a recent surface rupture ('not subset'). In total, 63 earthquake surface ruptures are included (Table 1), with data counted in either single or multiple sections and either subset or not subset. For example, a slip distribution from a recent rupture with two fault sections generates three datapoints: one for the entire fault, one for section 1, and one for section 2. Spatial variability for the entire fault is included in three groups: 'all data'; 'multiple sections'; and 'not subset'. Spatial variability for section 1 is included in 'all data', 'single section', and 'not subset'.

2.2 | Numerical landscape evolution model

To constrain the amount of spatial variability introduced by interpretation (introduced variability), we measure offset distances recorded in geomorphic markers in numerical landscape evolution models that simulate a strike-slip fault with constant slip along the fault (Figure 4), and calculate spatial variability [Equation (1)] using the coefficient of variation of all offset measurements in each simulation (Figure 5). We use the landscape evolution models published by Reitman et al. (2019b) that simulate geomorphic evolution of a strike-slip fault zone with discrete earthquakes on a single, linear strike-slip fault (Figure 4a), and build on the results with further processing, analysis, and interpretation. Change in landscape elevation with time was modelled using a Python program (Reitman et al., 2019a) written using Landlab (Barnhart et al., 2020a; Hobley et al., 2017). The models were designed as a simplified representation of a hypothetical strike-slip landscape with a climate similar to that of southern California. Channels are approximately linear, with flow direction normal to the fault

TABLE 1 Surface slip distribution data measured by hand

Most recent earthquake	Year	Fault (section)	*n*	Mean	Std	CV	$CV_{reported}$	CV_{corr}	Measured on	Subset?	Offset data froma	Events	Segments
Garlock prehistoric		Garlock (central & eastern)	164	3.13	1.08	0.35	0.36		field	yes	McGill and Sieh (1991)	single	multiple
Garlock prehistoric		Garlock (El Paso Mountains)	20	5.03	2.18	0.43	0.31		field	yes	McGill and Sieh (1991)	single	single
Garlock prehistoric		Garlock (Searles Valley)	17	2.65	0.96	0.36	0.38		field	yes	McGill and Sieh (1991)	single	single
Garlock prehistoric		Garlock (Pilot Knob Valley)	38	3.31	0.84	0.25	0.28		field	yes	McGill and Sieh (1991)	single	single
Garlock prehistoric		Garlock (Leach Lake & Avawatz Mtns)	91	2.96	1.04	0.35	0.42		field	yes	McGill and Sieh (1991)	single	single
Burgar Co prehistoric		Burgar Co	19	1.72	0.41	0.24	0.29		field & imagery	yes	Han et al. (2019)	single	single
Longriqu prehistoric		Longriqu	19	4.87	1.49	0.31	0.36		imagery	yes	Ansberque et al. (2016)	single	multiple
West Henlanshan prehistoric		West Henlanshan	12	2.51	0.42	0.17	0.14		stereo & sfm dems	yes	Bi et al. (2020)	single	multiple
AT eastern prehistoric		Altyn Tagh (eastern)	123	5.79	1.12	0.19	0.19		lidar	yes	Kang et al. (2020)	single	multiple
Tianjingshan prehistoric	~1.2 ± 0.1 kyr BP	Tianjingshan (western)	136	2.74	0.94	0.34	0.27		field, imagery, sfm dem	yes	Li et al. (2017)	single	multiple
AT Karakax prehistoric	<1020	Altyn Tagh (Karakax)	105	6.57	1.98	0.30	0.33		field & imagery	yes	Li et al. (2012)	single	single
AT Xorkoli 1270–1775	1270–1775	Altyn Tagh (Suoerkuli)	43	3.19	0.44	0.14	0.14		imagery	yes	Han et al. (2018)	single	single
AT Xorkoli 1270–1775	1270–1775	Altyn Tagh (Gebiling-Xorkoli)	35	7.34	1.01	0.14	0.14		imagery & sfm dem	yes	Xiong and Li (2020)	single	single
AT 676–1347	676–1347	Altyn Tagh (Annaba & Suoerkuli)	77	5.47	0.90	0.16	0.18		imagery	yes	Han et al. (2018)	single	multiple
AT 676–1347	676–1347	Altyn Tagh (Xorxoli)	70	5.54	1.24	0.22	0.22		field & imagery	yes	Elliott et al. (2015)	single	multiple
Yishu	1668	Yishu	188	8.65	1.40	0.16	0.16		imagery	yes	Jiang et al. (2017)	single	multiple
Anza	1800	San Jacinto (Clark strand)	209	2.29	0.92	0.40	0.34		field	yes	Salisbury et al. (2012)	single	multiple
Anza	1800	San Jacinto (Clark strand)	161	2.70	0.71	0.26	0.26		lidar	yes	Salisbury et al. (2012)	single	multiple
Marlborogh	1848	Awatere	38	5.61	1.66	0.30	0.31		field	yes	Mason and Little (2006)	single	single
Wairarapa	1855	Wairarapa	261	9.96	4.38	0.44	0.44		lidar	yes	Manighetti et al. (2020)	single	multiple
Fort Tejon	1857	San Andreas	220	4.60	1.59	0.35	0.46		lidar	yes	Zielke et al. (2012)	single	multiple
Fort Tejon	1857	San Andreas (Carrizo Plain)	46	5.31	0.74	0.14	0.14		lidar	yes	Zielke et al. (2010)	single	single
Owens Valley	1872	Owens Valley	112	3.27	1.53	0.47	0.47		field & lidar	yes	Haddon et al. (2016)	single	multiple
Jingtai	1888	Haiyuan (Laohu Shan)	128	2.08	0.81	0.39	0.32		field & lidar	yes	Chen et al. (2018)	single	single

TABLE 1 (Continued)

Most recent earthquake	Year	Fault (section)	*n*	Mean	Std	CV	$CV_{reported}$	CV_{corr}	Measured on	Subset?	Offset data froma	Events	Segments
North Canterbury	1888	Hope (eastern)	20	3.92	0.73	0.19	0.17		lidar	yes	Manighetti et al. (2015a)	single	single
Nobi	1891	Neo-Dani	30	3.41	2.18	0.64	0.70		SURE database	no	Baize et al. (2019)	single	multiple
Nobi	1891	Neo-Dani	19	3.77	2.19	0.58	0.71		Wesnousky digitized	no	Wesnousky (2008)	single	multiple
Bulnay	1905	Bulnay	231	6.01	2.20	0.37	0.35		imagery	no	Choi et al. (2018)	single	multiple
Bulnay	1905	Bulnay	26	4.22	0.51	0.12			imagery	no	Choi et al. (2018)	single	single
Bulnay	1905	Bulnay	32	5.89	1.41	0.24			imagery	no	Choi et al. (2018)	single	single
Bulnay	1905	Bulnay	21	5.89	1.96	0.44			imagery	no	Choi et al. (2018)	single	single
Bulnay	1905	Bulnay	22	4.06	1.40	0.34			imagery	no	Choi et al. (2018)	single	single
Bulnay	1905	Bulnay	41	6.91	1.11	0.16			imagery	no	Choi et al. (2018)	single	single
Bulnay	1905	Bulnay	44	7.89	1.97	0.25			imagery	no	Choi et al. (2018)	single	single
Bulnay	1905	Bulnay	18	8.25	1.73	0.21			imagery	no	Choi et al. (2018)	single	single
Bulnay	1905	Teregtiyn	21	3.03	0.80	0.26	0.28		imagery	no	Choi et al. (2018)	single	single
Tsetserleg	1905	Tsetserleg	22	2.49	0.60	0.24	0.25		imagery	no	Choi et al. (2018)	single	multiple
San Francisco	1906	San Andreas	36	3.00	1.47	0.49			Lin compilation	no	Lin et al. (2020)	single	multiple
Haiyuan	1920	Haiyuan	119	3.61	1.66	0.46	0.48		lidar	yes	Ren et al. (2016)	single	multiple
Haiyuan	1920	Haiyuan	146	3.37	0.98	0.29	0.28		imagery	yes	Ou et al. (2020)	single	multiple
Gulang	1927	Lenglongling	83	4.91	1.47	0.30	0.31		field & imagery	yes	Guo et al. (2019)	single	single
Kitatango	1927	Gomura	168	1.24	0.91	0.73			SURE database	no	Baize et al. (2019)	single	multiple
Kitatango	1927	Gomura	67	1.12	0.96	0.86			Lin compilation	no	Lin et al. (2020)	single	multiple
Kita-Izu	1930	Kita-Izu	122	0.97	0.76	0.79	0.69		SURE database	no	Baize et al. (2019)	single	multiple
Kita-Izu	1930	Kita-Izu	45	1.59	0.98	0.62	0.89		Wesnousky digitized	no	Wesnousky (2008)	single	multiple
Fuyun	1931	Fuyun	348	6.05	1.46	0.24	0.23		imagery	yes	Klinger et al. (2011)	single	multiple
Fuyun	1931	Fuyun	32	6.78	2.39	0.35	0.38		field	no	Jianbang (1984)b	single	multiple
Fuyun	1931	Fuyun	73	6.32	1.99	0.31			field	no	Lin (1998)b	single	multiple
Erzincan	1939	North Anatolian	27	4.95	1.77	0.36	0.42		field	no	Barka (1996)	single	multiple
Erzincan	1939	North Anatolian	93	4.46	2.37	0.53	0.52		imagery, field	no	Emre et al. (2020)	single	multiple
Erzincan	1939	North Anatolian	36	2.41	0.63	0.26	0.28		imagery, field	no	Emre et al. (2020)	single	single
Erzincan	1939	North Anatolian	11	4.25	0.95	0.22	0.21		imagery, field	no	Emre et al. (2020)	single	single
Erzincan	1939	North Anatolian	20	5.40	1.34	0.25	0.25		imagery, field	no	Emre et al. (2020)	single	single
Erzincan	1939	North Anatolian	13	8.61	1.47	0.17	0.17		imagery, field	no	Emre et al. (2020)	single	single

TABLE 1 (Continued)

Most recent earthquake	Year	Fault (section)	*n*	Mean	Std	CV	$CV_{reported}$	CV_{corr}	Measured on	Subset?	Offset data froma	Events	Segments
Erzincan	1939	North Anatolian	13	4.70	1.77	0.38	0.48		imagery, field	no	Emre et al. (2020)	single	single
Imperial Valley	1940	Imperial	107	4.73	1.16	0.24	0.21		imagery	no	Rockwell and Klinger (2013)	single	single
Imperial Valley	1940	Imperial	502	0.95	0.46	0.49	0.46		imagery	no	Rockwell and Klinger (2013)	single	single
Imperial Valley	1940	Imperial	609	1.62	1.58	0.97	0.99		imagery	no	Rockwell and Klinger (2013)	single	multiple
Niksar-Erbaa	1942	North Anatolian	10	1.40	0.55	0.39	0.33		field	no	Barka (1996)	single	multiple
Tottori	1943	Shikano	37	0.45	0.35	0.77			SURE database	no	Baize et al. (2019)	single	multiple
Tottori	1943	Shikano & Yoshikoa	20	0.47	0.39	0.81	0.64		Wesnousky digitized	no	Wesnousky (2008)	single	multiple
Tottori	1943	Shikano	8	0.60	0.47	0.78			Wesnousky digitized	no	Wesnousky (2008)	single	single
Tottori	1943	Yoshikoa	12	0.39	0.31	0.80			Wesnousky digitized	no	Wesnousky (2008)	single	single
Tosya	1943	North Anatolian	18	2.32	0.97	0.42	0.39		field	no	Barka (1996)	single	multiple
Bolu-Gerede	1944	North Anatolian	54	3.22	1.45	0.45	0.43		field	no	Kondo et al. (2005)	single	multiple
Bolu-Gerede	1944	North Anatolian	34	3.43	1.39	0.41	0.41		field	no	Kondo et al. (2005)	single	multiple
Gobi-Altay	1957	Bogd	31	4.05	0.81	0.20	0.23		field	yes	Rizza et al. (2011)	single	single
Gobi-Altay	1957	Bogd	24	4.15	1.79	0.43	0.51		field	no	Kurushin et al. (1997)	single	multiple
Gobi-Altay	1957	Bogd	184	2.95	1.50	0.51	0.43		field	no	Choi et al. (2012)	single	multiple
Gobi-Altay	1957	Bogd	147	3.02	1.41	0.47	0.40		field	no	Choi et al. (2012)	single	multiple
Gobi-Altay	1957	Bogd	1018	3.46	1.03	0.30	0.29		imagery	yes	Kurtz et al. (2018)	single	multiple
Mudurnu Valley	1967	North Anatolian	21	0.80	0.53	0.66	0.58		field	no	Barka (1996)	single	multiple
Borrego Mountain	1968	Coyote Creek	46	0.10	0.12	1.24	0.96		field	no	Clark (1972)	single	multiple
Borrego Mountain	1968	Coyote Creek	16	0.21	0.14	0.66	0.70		field	no	Clark (1972)	single	single
Borrego Mountain	1968	Coyote Creek	11	0.08	0.08	0.95	1.03		field	no	Clark (1972)	single	single
Borrego Mountain	1968	Coyote Creek	18	0.02	0.02	1.24	0.76		field	no	Clark (1972)	single	single
Izu-Hando-Oki	1974		23	0.23	0.22	0.98			SURE database	no	Baize et al. (2019)	single	multiple
Izu-Hando-Oki	1974		15	0.28	0.13	0.45			Lin compilation	no	Lin et al. (2020)	single	multiple
Guatemala	1976	Motagua	73	1.04	0.55	0.53	0.51		field	no	Plafker (1976)	single	single
Bob-Tangol	1977	Kuh Banan (Bob Tongol)	35	0.05	0.04	0.84	0.87		field?	no	Berberian et al. (1979)	single	single

TABLE 1 (Continued)

Most recent earthquake	Year	Fault (section)	*n*	Mean	Std	CV	$CV_{reported}$	CV_{corr}	Measured on	Subset?	Offset data froma	Events	Segments
Imperial Valley	1979	Imperial	37	0.34	0.17	0.50	0.59		field	no	Sharp (1982)	single	single
Imperial Valley	1979	Imperial	37	0.39	0.18	0.47			field	no	Sharp (1982)	single	single
Imperial Valley	1979	Imperial	37	0.42	0.19	0.45			field	no	Sharp (1982)	single	single
Imperial Valley	1979	Imperial	37	0.49	0.20	0.41	0.47		field	no	Sharp (1982)	single	single
Sirch	1981	Gowk	38	0.11	0.11	1.01	1.13		field	no	Berberian et al. (1984, 2001)	single	multiple
Superstition Hills	1987	Superstition Hills	53	0.27	0.14	0.53	0.41		field	no	Sharp et al. (1989)	single	multiple
Superstition Hills	1987	Superstition Hills	38	0.58	0.14	0.24	0.23		field	no	Lindvall et al. (1989)	single	multiple
Luzon	1990	Philippine	48	3.35	1.50	0.45	0.50		field	no	Nakata et al. (1990)	single	multiple
Luzon	1990	Philippine	19	4.42	1.09	0.25	0.20		field	no	Nakata et al. (1990)	single	single
Luzon	1990	Philippine	29	2.65	1.31	0.49	0.65		field	no	Nakata et al. (1990)	single	single
Landers	1992	Emerson	60	3.16	1.10	0.35	0.37		field	no	McGill and Rubin (1999)	single	single
Landers	1992	All	78	2.78	1.66	0.60	0.72	0.40	Wesnousky digitized	no	Wesnousky (2008)	single	multiple
Landers	1992	Johnson Valley	15	1.78	0.65	0.36			Wesnousky digitized	no	Wesnousky (2008)	single	single
Landers	1992	Homestead Valley North	13	2.28	1.02	0.44			Wesnousky digitized	no	Wesnousky (2008)	single	single
Landers	1992	Emerson	21	3.75	1.71	0.46			Wesnousky digitized	no	Wesnousky (2008)	single	single
Kobe (Hyogo-ken Nanbu)	1995	Nojima & Suwayama	58	1.11	0.53	0.48	0.38		field?	no	Awata et al. (1996)	single	multiple
Zirkuh	1997	Abiz	83	0.92	0.63	0.68	0.31		field	no	Berberian et al. (1999)	single	multiple
Fandoqa (Kerman)	1998	Gowk	22	0.99	0.95	0.96	0.73		field	no	Berberian et al. (2001)	single	multiple
Hector Mine	1999	All	255	2.27	1.32	0.58	0.56	0.49	lidar	no	Chen et al. (2015)	single	multiple
Hector Mine	1999	Lavic Lake	217	2.43	1.32	0.55	0.56		lidar	no	Chen et al. (2015)	single	single
Hector Mine	1999	Lavic Lake & West Bullion	130	1.66	1.35	0.82	0.54		field	no	Treiman et al. (2002)	single	multiple
Izmit	1999	North Anatolian (all Izmit)	119	1.75	1.26	0.72	0.63		field	no	Barka et al. (2002)	single	multiple
Izmit	1999	North Anatolian (Izmit-Sapanca Lake)	23	2.11	0.54	0.26	0.22		field	no	Barka et al. (2002)	single	single
Izmit	1999	North Anatolian (Karadere)	28	0.77	0.47	0.61	0.39		field	no	Barka et al. (2002)	single	single
Izmit	1999	North Anatolian (Sapanca-Akyazi)	58	1.99	1.44	0.72	0.58		field	no	Barka et al. (2002)	single	single
Duzce	1999	North Anatolian (Duzce)	70	2.39	1.23	0.51	0.41		field	no	Akyüz et al. (2002)	single	single
Kokoxili	2001	Kunlun (Kusai Hu)	83	4.71	1.70	0.36	0.31		imagery & field	no	Klinger et al. (2005)	single	single
Denali	2002	Denali	109	4.52	1.81	0.40	0.41		field	no	Haeussler et al. (2004a)	single	single

TABLE 1 (Continued)

Most recent earthquake	Year	Fault (section)	*n*	Mean	Std	CV	$CV_{reported}$	CV_{corr}	Measured on	Subset?	Offset data from[a]	Events	Segments
Denali	2002	Denali & Totschunda	127	4.15	1.96	0.47	0.53		field	no	Haeussler et al. (2004b)	single	
Denali	2002	Totschunda	18	1.73	0.78	0.45	0.49		field	no	Haeussler et al. (2004b)	single	single
Darfield	2010	Greendale	27	2.23	1.17	0.53	0.47		field	no	Elliott et al. (2012)	single	multiple
Darfield	2010	Greendale	56	2.47	1.45	0.59	0.58		imagery	no	Elliott et al. (2012)	single	multiple
Darfield	2010	Greendale	53	2.74	1.34	0.49	0.54		imagery	no	Elliott et al. (2012)	single	multiple
El Mayor-Cucapah	2010	All Sierra Domain	574	0.72	0.80	1.11	0.40		field	no	Fletcher et al. (2014)	single	multiple
El Mayor-Cucapah	2010	Paso Superior	155	0.53	0.60	1.13	0.39		field	no	Fletcher et al. (2014)	single	multiple
El Mayor-Cucapah	2010	Paso Inferior	230	0.78	0.87	1.12	0.31		field	no	Fletcher et al. (2014)	single	multiple
El Mayor-Cucapah	2010	Borrego	58	0.58	0.45	0.78	0.25		field	no	Fletcher et al. (2014)	single	single
El Mayor-Cucapah	2010	Pescadores	46	1.62	0.96	0.59	0.39		field	no	Fletcher et al. (2014)	single	single
El Mayor-Cucapah	2010	Laguna Salada	59	0.60	0.67	1.12	0.33		field	no	Fletcher et al. (2014)	single	single
Pisayambo	2010	Laguna Pisayambo	11	0.36	0.16	0.44	0.62		field	no	Baize et al. (2019); Champenois et al. (2017)	single	single
Yushu	2010	Yushu	47	1.22	0.64	0.52	0.43		field	no	Lin et al. (2011)	single	single
Tarlay	2011	Nam Ma	43	0.65	0.34	0.52	0.42		field	no	Tun et al. (2014)	single	single
Tarlay	2011	Nam Ma	43	1.43	0.36	0.25	0.44		imagery	no	Tun et al. (2014)	single	single
Balochistan	2013	Hoshab	308	6.47	2.81	0.43	0.43	0.33	imagery	no	Gold et al. (2015)	single	multiple
Balochistan	2013	Hoshab	258	7.99	2.89	0.36	0.34		imagery	no	Gold et al. (2015)	single	multiple
South Napa	2014	West Napa	131	0.09	0.10	1.08	0.67		field	no	Ponti et al. (2019)	single	multiple
South Napa	2014	West Napa	67	0.15	0.11	0.75	0.75		field	no	Ponti et al. (2019)	single	single
Yutian	2014	Altyn Tagh	28	0.50	0.25	0.50	0.50		field	no	Li et al. (2016)	single	multiple
Kaikoura	2016	Upper Kowhai, Manakau, Kekerengu, Jordan, Needles	98	7.14	2.82	0.40	0.54		field & lidar	no	Kearse et al. (2018)	single	multiple
Kaikoura	2016	Kekerengu	69	7.62	2.76	0.36	0.53	0.24	field & lidar	no	Kearse et al. (2018)	single	single
Kumamoto	2016	Hinagu & Fugawa	145	0.61	0.49	0.80	0.69	0.70	field	no	Shirahama et al. (2016)	single	multiple
Kumamoto	2016	Hinagu	31	0.41	0.17	0.43	0.58		field	no	Shirahama et al. (2016)	single	single
Kumamoto	2016	Fugawa	114	0.66	0.53	0.80	0.76		field	no	Shirahama et al. (2016)	single	multiple
Ridgecrest 6.4	2019	Salt Wells Valley (all strands)	75	0.31	0.40	1.32	1.00	0.78	field	no	DuRoss et al. (2020)	single	multiple
Ridgecrest 6.4	2019	Salt Wells Valley (strand 21)	48	0.43	0.45	1.04	1.13	0.58	field	no	DuRoss et al. (2020)	single	single
Ridgecrest 7.1	2019	Paxton Ranch (all strands)	264	1.23	1.28	1.05	1.07	0.78	field	no	DuRoss et al. (2020)	single	multiple
Ridgecrest 7.1	2019	Paxton Ranch (strand 1)	174	1.59	1.37	0.86	1.14	0.61	field	no	DuRoss et al. (2020)	single	single

(Continues)

TABLE 1 (Continued)

Most recent earthquake	Year	Fault (section)	*n*	Mean	Std	CV	$CV_{reported}$	CV_{corr}	Measured on	Subset?	Offset data froma	Events	Segments

[a]aFull citations are in the reference list.
[b]bData accessed from supplement to Klinger et al. (2011).

TABLE 1 (Continued)

Most recent earthquake	Rupture length (km)	Max slip (m)	Avg. slip (m)	Type	Measurement density (#/km)	% OFD	M_w	Epicentre latitude (WGS84)	Epicentre longitude (WGS84)	Notes	Epicentre location source
Garlock prehistoric	140	5.5	3	sinistral	1.17		7.2			measurements ≤5.5 m	no location data in McGill and Sieh (1991)
Garlock prehistoric	129	9	7	sinistral	0.16		7.2			measurements <9 m	no location data in McGill and Sieh (1991)
Garlock prehistoric	40	5	2.5	sinistral	0.43		7.2			measurements <5 m	no location data in McGill and Sieh (1991)
Garlock prehistoric	37	5	3	sinistral	1.03		7.2			measurements <5 m	no location data in McGill and Sieh (1991)
Garlock prehistoric	71	5.5	2.5	sinistral	1.28		7.2			measurements <5 m	no location data in McGill and Sieh (1991)
Burgar Co prehistoric	50	2.4	1.4	dextral	0.38		7.0	33.800	84.000	measurements <2.5 m	Approx. from map in Han et al. (2019)
Longriqu prehistoric	80	7.5	4.1	dextral	0.24		7.4	32.670	102.670	4.1 m cluster, multiple strands	Approx. from map in Ansberque et al. (2016)
West Henlanshan prehistoric	50	4	3	dextral	0.24		7.3	38.600	105.670	smallest cluster (<4 m)	Approx. from map in Bi et al. (2020)
AT eastern prehistoric	150	9	6	sinistral	0.82		7.6	39.860	96.120	smallest cluster (6 m, all measurements <8 m)	Kang et al. (2020) mean of measurement locations
Tianjingshan prehistoric	45	4	3.5	sinistral	3.02		7.3	37.500	104.250	3 m cluster (<5 m)	Approx. from map in Li et al. (2017)
AT Karakax prehistoric	55	10	6	sinistral	1.91		7.5	36.000	80.000	6 m cluster	Approx. from map in Li et al. (2012)
AT Xorkoli 1270–1775	140	4.15	3.12	sinistral	0.31		7.5	38.990	92.010	Suoerkuli segment (120–240 km distance)	Han et al. (2018) mean of measurement locations
AT Xorkoli 1270–1775	2	10	7.1	sinistral	17.50			38.700	90.940	smallest cluster (7 m)	Approx. from map in Xiong and Li (2020)
AT 676–1347	170	7.25	5	sinistral	0.45		7.6	38.990	92.010	penultimate event (5 m cluster, 4–7.25 m measurements)	Han et al. (2018) mean of measurement locations
AT 676–1347	45	8	5.6	sinistral	1.56		7.7	39.220	93.060	5 m cluster (measurements <8 m)	Elliott et al. (2015) mean of measurement locations

TABLE 1 (Continued)

Most recent earthquake	Rupture length (km)	Max slip (m)	Avg. slip (m)	Type	Measurement density (#/km)	% OFD	M_w	Epicentre latitude (WGS84)	Epicentre longitude (WGS84)	Notes	Epicentre location source
Yishu	270	13	9	dextral	0.70		8.5	35.300	118.600	9 m cluster	https://en.wikipedia.org/wiki/1668_Shandong_earthquake
Anza	80	4	2.7	dextral	2.61		7.4	33.570	−116.580	field measurements ≤4 m	Salisbury et al. (2012) measurements approx. centroid
Anza	80	4	2.7	dextral	2.01		7.4	33.570	−116.580	lidar measurements ≤4 m	Salisbury et al. (2012) measurements approx. centroid
Marlborogh	110	7	5.3	dextral	0.35		7.5	−41.800	173.700	single event measurements only	https://en.wikipedia.org/wiki/1848_Marlborough_earthquake
Wairarapa	70	18.6	10	dextral	3.73		8.2	−41.200	175.200	smallest cluster (<19 m)	https://en.wikipedia.org/wiki/1855_Wairarapa_earthquake
Fort Tejon	350	6	3.5	dextral	0.63		7.9	35.700	−120.300	data likely from 1857 earthquake	https://earthquake.usgs.gov/earthquakes/eventpage/ushis92/executive
Fort Tejon	60	7.5	5.3	dextral	0.77		7.9	35.700	−120.300	data from 5 m cluster only	https://earthquake.usgs.gov/earthquakes/eventpage/ushis92/executive
Owens Valley	110	6	3.3	dextral	1.02		7.4	36.700	−118.100	data from 3.3 m cluster only	https://earthquake.usgs.gov/earthquakes/eventpage/ushis161/executive
Jingtai	52	4	2.5	sinistral	2.46		8.0	37.110	103.730	≤4 m cluster, includes creep	Chen et al. (2018) measurements approx. centroid
North Canterbury	30	6	4.2	dextral	0.67		7.2	−42.600	172.400	smallest cluster (<6 m)	https://en.wikipedia.org/wiki/1888_North_Canterbury_earthquake
Nobi	80	7.9	3.1	sinistral	0.38		7.5	35.600	136.600	offset data taken from SURE database	Fukuyama et al. (2007); https://en.wikipedia.org/wiki/1891_Mino%E2%80%93Owari_earthquake
Nobi	80	7.9	3.1	sinistral	0.24		7.5	35.600	136.600	left-lateral only, >0, offset data taken from Wesnousky (2008)	Fukuyama et al. (2007); https://en.wikipedia.org/wiki/1891_Mino%E2%80%93Owari_earthquake
Bulnay	388	10	6.37	sinistral	0.60		8.4	49.369	96.610	all 11 sections of the Bulnay fault	https://earthquake.usgs.gov/earthquakes/eventpage/iscgem16957865/executive
Bulnay				sinistral			8.4	49.369	96.610	section B	https://earthquake.usgs.gov/earthquakes/eventpage/iscgem16957865/executive

TABLE 1 (Continued)

Most recent earthquake	Rupture length (km)	Max slip (m)	Avg. slip (m)	Type	Measurement density (#/km)	% OFD	M_w	Epicentre latitude (WGS84)	Epicentre longitude (WGS84)	Notes	Epicentre location source
Bulnay				sinistral			8.4	49.369	96.610	section C	https://earthquake.usgs.gov/earthquakes/eventpage/iscgem16957865/executive
Bulnay				sinistral			8.4	49.369	96.610	section D	https://earthquake.usgs.gov/earthquakes/eventpage/iscgem16957865/executive
Bulnay				sinistral			8.4	49.369	96.610	section E	https://earthquake.usgs.gov/earthquakes/eventpage/iscgem16957865/executive
Bulnay				sinistral			8.4	49.369	96.610	section F	https://earthquake.usgs.gov/earthquakes/eventpage/iscgem16957865/executive
Bulnay				sinistral			8.4	49.369	96.610	section G	https://earthquake.usgs.gov/earthquakes/eventpage/iscgem16957865/executive
Bulnay				sinistral			8.4	49.369	96.610	section H	https://earthquake.usgs.gov/earthquakes/eventpage/iscgem16957865/executive
Bulnay	80	4	2.9	sinistral	0.26		8.4	49.369	96.610	Teregtiyn fault	https://earthquake.usgs.gov/earthquakes/eventpage/iscgem16957865/executive
Tsetserleg	114	3	2.34	sinistral	0.19		8.0	49.709	98.483	Tsetserleg fault	https://earthquake.usgs.gov/earthquakes/eventpage/iscgem16957859/executive
San Francisco				dextral			7.9	37.750	−122.550	offset data taken from Lin et al. (2020)	https://earthquake.usgs.gov/earthquakes/eventpage/official19060418131226300_12/executive
Haiyuan	140	6	3.5	sinistral	0.85		7.9	36.888	105.606	smallest cluster	https://earthquake.usgs.gov/earthquakes/eventpage/iscgem912687/executive
Haiyuan	160	6	3.5	sinistral	0.91		7.9	36.888	105.606	smallest cluster (0–5 m), all sections	https://earthquake.usgs.gov/earthquakes/eventpage/iscgem912687/executive
Gulang	120	7	4.8	sinistral	0.69		7.7	37.645	102.489	max 7 m cluster	https://earthquake.usgs.gov/earthquakes/eventpage/iscgem909273/executive

TABLE 1 (Continued)

Most recent earthquake	Rupture length (km)	Max slip (m)	Avg. slip (m)	Type	Measurement density (#/km)	% OFD	M_w	Epicentre latitude (WGS84)	Epicentre longitude (WGS84)	Notes	Epicentre location source
Kitatango				both			7.1	35.632	135.013	>0, offset data taken from SURE database	https://earthquake.usgs.gov/earthquakes/eventpage/iscgem909128/executive
Kitatango				both			7.1	35.632	135.013	offset data taken from Lin et al. (2020)	https://earthquake.usgs.gov/earthquakes/eventpage/iscgem909128/executive
Kita-Izu	35	3.5	1.1	sinistral	3.49		6.9	35.050	139.129	>0, offset data taken from SURE database	https://earthquake.usgs.gov/earthquakes/eventpage/iscgem907761/executive
Kita-Izu	35	3.5	1.1	sinistral	1.29		6.9	35.050	139.129	>0, offset data taken from Wesnousky (2008) digitized data	https://earthquake.usgs.gov/earthquakes/eventpage/iscgem907761/executive
Fuyun	110	12	6.3	dextral	3.16		8.0	46.817	89.915	data from 6 m cluster only	https://earthquake.usgs.gov/earthquakes/eventpage/iscgem906933/executive
Fuyun	115	14	6.3	dextral	0.28		8.0	46.817	89.915	1931 field data	https://earthquake.usgs.gov/earthquakes/eventpage/iscgem906933/executive
Fuyun				dextral			8.0	46.817	89.915	1931 field data	https://earthquake.usgs.gov/earthquakes/eventpage/iscgem906933/executive
Erzincan	360	7.4	4.2	dextral	0.08		7.8	39.771	39.577	all	https://earthquake.usgs.gov/earthquakes/eventpage/iscgem902291/executive
Erzincan	330	10.5	4.58	dextral	0.28		7.8	39.771	39.577	all	https://earthquake.usgs.gov/earthquakes/eventpage/iscgem902291/executive
Erzincan	76	3.7	2.27	dextral	0.47		7.8	39.771	39.577	Enzinepazari	https://earthquake.usgs.gov/earthquakes/eventpage/iscgem902291/executive
Erzincan	90	5.3	4.4	dextral	0.12		7.8	39.771	39.577	Resadiye	https://earthquake.usgs.gov/earthquakes/eventpage/iscgem902291/executive
Erzincan	65	7.8	5.45	dextral	0.31		7.8	39.771	39.577	Susehri	https://earthquake.usgs.gov/earthquakes/eventpage/iscgem902291/executive
Erzincan	49	10.5	8.8	dextral	0.27		7.8	39.771	39.577	Refahiye	

(Continues)

TABLE 1 (Continued)

Most recent earthquake	Rupture length (km)	Max slip (m)	Avg. slip (m)	Type	Measurement density (#/km)	% OFD	M_w	Epicentre latitude (WGS84)	Epicentre longitude (WGS84)	Notes	Epicentre location source
											https://earthquake.usgs.gov/earthquakes/eventpage/iscgem902291/executive
Erzincan	42	7.25	3.67	dextral	0.31		7.8	39.771	39.577	Erzincan	https://earthquake.usgs.gov/earthquakes/eventpage/iscgem902291/executive
Imperial Valley	4	7	5.5	dextral	26.75		7.0	32.844	−115.381	0–4 km segment	https://earthquake.usgs.gov/earthquakes/eventpage/iscgem901341/executive
Imperial Valley	10	2	1	dextral	50.20		7.0	32.844	−115.381	4–14 km segment	https://earthquake.usgs.gov/earthquakes/eventpage/iscgem901341/executive
Imperial Valley	14	7	1.6	dextral	43.50		7.0	32.844	−115.381	all measurements, excluding zeros	https://earthquake.usgs.gov/earthquakes/eventpage/iscgem901341/executive
Niksar-Erbaa	50	1.9	1.66	dextral	0.20		6.8	40.870	36.732	all	https://earthquake.usgs.gov/earthquakes/eventpage/iscgem900592/executive
Tottori				sinistral			6.7	35.448	133.993	offset data taken from SURE database	https://earthquake.usgs.gov/earthquakes/eventpage/iscgem899991/executive
Tottori	10.5	1.5	0.6	sinistral	1.90		6.7	35.448	133.993	offset data taken from Wesnousky (2008)	https://earthquake.usgs.gov/earthquakes/eventpage/iscgem899991/executive
Tottori				sinistral			6.7	35.448	133.993	offset data taken from Wesnousky (2008)	https://earthquake.usgs.gov/earthquakes/eventpage/iscgem899991/executive
Tottori				sinistral			6.7	35.448	133.993	offset data taken from Wesnousky (2008)	https://earthquake.usgs.gov/earthquakes/eventpage/iscgem899991/executive
Tosya	260	4.4	2.5	dextral	0.07		7.6	40.916	33.562	all	https://earthquake.usgs.gov/earthquakes/eventpage/iscgem900102/executive
Bolu-Gerede	170	6.3	3.4	dextral	0.32		7.4	40.696	32.992	all measurements (good and poor quality)	https://earthquake.usgs.gov/earthquakes/eventpage/iscgem899277/executive
Bolu-Gerede	170	6.3	3.4	dextral	0.20		7.4	40.696	32.992	good measurements only	

(Continues)

TABLE 1 (Continued)

Most recent earthquake	Rupture length (km)	Max slip (m)	Avg. slip (m)	Type	Measurement density (#/km)	% OFD	M_w	Epicentre latitude (WGS84)	Epicentre longitude (WGS84)	Notes	Epicentre location source
											https://earthquake.usgs.gov/earthquakes/eventpage/iscgem899277/executive
Gobi-Altay	260	6	3.5	sinistral	0.12		8.1	45.189	99.368	<6 m cluster	https://earthquake.usgs.gov/earthquakes/eventpage/iscgem887636/executive
Gobi-Altay	260	6	3.5	sinistral	0.09		8.1	45.189	99.368	excludes zeros and negatives	https://earthquake.usgs.gov/earthquakes/eventpage/iscgem887636/executive
Gobi-Altay	260	6	3.5	sinistral	0.71		8.1	45.189	99.368	all measurements	https://earthquake.usgs.gov/earthquakes/eventpage/iscgem887636/executive
Gobi-Altay	260	6	3.5	sinistral	0.57		8.1	45.189	99.368	good measurements only	https://earthquake.usgs.gov/earthquakes/eventpage/iscgem887636/executive
Gobi-Altay	260	6	3.5	sinistral	3.92		8.1	45.189	99.368	smallest cluster (<5.5 m)	https://earthquake.usgs.gov/earthquakes/eventpage/iscgem887636/executive
Mudurnu Valley	80	2	0.9	dextral	0.26		7.4	40.751	30.800	all	https://earthquake.usgs.gov/earthquakes/eventpage/iscgem833573/executive
Borrego Mountain	31	0.38	0.13	dextral	1.48		6.6	33.180	−116.103	all co-siesmic	https://earthquake.usgs.gov/earthquakes/eventpage/ci3329122/executive
Borrego Mountain	13	0.38	0.2	dextral	1.23		6.6	33.180	−116.103	north segment, co-seismic	https://earthquake.usgs.gov/earthquakes/eventpage/ci3329122/executive
Borrego Mountain	11	0.2	0.075	dextral	1.00		6.6	33.180	−116.103	central segment, co-seismic	https://earthquake.usgs.gov/earthquakes/eventpage/ci3329122/executive
Borrego Mountain	7	0.08	0.03	dextral	2.57		6.6	33.180	−116.103	south segment, co-seismic	https://earthquake.usgs.gov/earthquakes/eventpage/ci3329122/executive
Izu-Hando-Oki				dextral			6.5	34.522	138.740	offset data taken from SURE database	https://earthquake.usgs.gov/earthquakes/eventpage/iscgem748001/executive
Izu-Hando-Oki				dextral			6.5	34.522	138.740		

(Continues)

TABLE 1 (Continued)

Most recent earthquake	Rupture length (km)	Max slip (m)	Avg. slip (m)	Type	Measurement density (#/km)	% OFD	M_w	Epicentre latitude (WGS84)	Epicentre longitude (WGS84)	Notes	Epicentre location source
										offset data taken from Lin et al. (2020)	https://earthquake.usgs.gov/earthquakes/eventpage/iscgem748001/executive
Guatemala	230	3.4	1.08	sinistral	0.32		7.5	15.324	−89.101	no mention of segmentation	https://earthquake.usgs.gov/earthquakes/eventpage/iscgem717474/executive
Bob-Tangol	19.5	0.2	0.05	dextral	1.79		5.8	30.954	56.473	all	https://earthquake.usgs.gov/earthquakes/eventpage/usp0000s58/executive
Imperial Valley	30.5	0.555	0.29	dextral	1.21		6.5	32.667	−115.359	4 days after earthquake, >0	https://earthquake.usgs.gov/earthquakes/eventpage/ci3352060/executive
Imperial Valley	30.5			dextral	1.21		6.5	32.667	−115.359	10 days after earthquake, >0	https://earthquake.usgs.gov/earthquakes/eventpage/ci3352060/executive
Imperial Valley	30.5			dextral	1.21		6.5	32.667	−115.359	20 days after earthquake, >0	https://earthquake.usgs.gov/earthquakes/eventpage/ci3352060/executive
Imperial Valley	30.5	0.78	0.43	dextral	1.21		6.5	32.667	−115.359	160 days after earthquake, >0	https://earthquake.usgs.gov/earthquakes/eventpage/ci3352060/executive
Sirch	63	0.43	0.1	dextral	0.60		7.1	30.013	57.794		https://earthquake.usgs.gov/earthquakes/eventpage/iscgem624412/executive
Superstition Hills	27	0.5	0.35	dextral	1.96		6.6	33.015	−115.852	all, 1 day after earthquake, no afterslip	https://earthquake.usgs.gov/earthquakes/eventpage/ci628016/executive
Superstition Hills	22.5	0.8	0.6	dextral	1.69		6.6	33.015	−115.852	1987 only, includes afterslip	https://earthquake.usgs.gov/earthquakes/eventpage/ci628016/executive
Luzon	110	6	3	sinistral	0.44		7.6	15.679	121.172	all	https://earthquake.usgs.gov/earthquakes/eventpage/iscgem362868/executive
Luzon	60	6	5.5	sinistral	0.32		7.6	15.679	121.172	20–80 km	https://earthquake.usgs.gov/earthquakes/eventpage/iscgem362868/executive
Luzon	50	2.5	2	sinistral	0.58		7.6	15.679	121.172	−30 to 20 km	

(Continues)

TABLE 1 (Continued)

Most recent earthquake	Rupture length (km)	Max slip (m)	Avg. slip (m)	Type	Measurement density (#/km)	% OFD	M_w	Epicentre latitude (WGS84)	Epicentre longitude (WGS84)	Notes	Epicentre location source
											https://earthquake.usgs.gov/earthquakes/eventpage/iscgem362868/executive
Landers	5.6	5.3	3	dextral	10.71		7.3	34.200	−116.437	summed across fault strands	https://earthquake.usgs.gov/earthquakes/eventpage/ci3031111/executive
Landers	85	6	2.3	dextral	0.92	0.46	7.3	34.200	−116.437	cumulative slip from all strands. Data from Wesnousky (2008)	https://earthquake.usgs.gov/earthquakes/eventpage/ci3031111/executive
Landers				dextral			7.3	34.200	−116.437		https://earthquake.usgs.gov/earthquakes/eventpage/ci3031111/executive
Landers				dextral			7.3	34.200	−116.437		https://earthquake.usgs.gov/earthquakes/eventpage/ci3031111/executive
Landers				dextral			7.3	34.200	−116.437		https://earthquake.usgs.gov/earthquakes/eventpage/ci3031111/executive
Kobe (Hyogo-ken Nanbu)	12	2.1	1.4	dextral	4.83		6.9	34.583	135.018	all lateral >0 (from Petersen et al., 2011)	https://earthquake.usgs.gov/earthquakes/eventpage/usp0006rew/executive
Zirkuh	125	2.3	2	dextral	0.66		7.2	33.825	59.809	all >0	https://earthquake.usgs.gov/earthquakes/eventpage/usp000820p/executive
Fandoqa (Kerman)	23	3	1.3	dextral	0.96		6.6	30.154	57.605	all Fandoqa	https://earthquake.usgs.gov/earthquakes/eventpage/usp0008hg7/executive
Hector Mine	43	6.6	2.37	dextral	5.93	0.39	7.1	34.603	−116.265		https://earthquake.usgs.gov/earthquakes/eventpage/ci9108652/executive
Hector Mine	43	6.6	2.37	dextral	5.05		7.1	34.603	−116.265		https://earthquake.usgs.gov/earthquakes/eventpage/ci9108652/executive
Hector Mine	48	5.2	2.5	dextral	2.71		7.1	34.603	−116.265	main strand, >0, excluding minimums	https://earthquake.usgs.gov/earthquakes/eventpage/ci9108652/executive
Izmit	145	5.2	2	dextral	0.82		7.6	40.748	29.864	all segments	

(Continues)

TABLE 2 Surface slip distribution data measured from image correlation

Earthquake	Year	Fault	n	Mean	Std	CV_{corr}	Rupture length (km)	M_w	Measurement density (#/km)	% OFD	Measured by	Data from[a]	Notes
Landers	1992	all	237	2.72	1.24	0.40	60	7.3	4.0	46%	image correlation	Milliner et al. (2016b)	image correlation, sum of all strands
Hector Mine	1999	all	470	2.87	1.64	0.49	48	7.1	9.8	39%	image correlation	Milliner et al. (2016b)	image correlation, sum of all strands
Balochistan	2013	Hoshab	330	8.29	2.73	0.33	200	7.7	1.7	28%	image correlation	Gold et al. (2015)	far-field, image correlation
Kumamoto	2016	Hinagu & Fugawa	264	2.39	1.66	0.70	34	7.0	7.8	50%	lidar, optical, insar	Scott et al. (2019)	all RL > 0, includes many outliers
Kaikoura	2016	Kekerengu	53	9.47	2.37	0.24	13.5	7.8	3.9	36%	image correlation	Zinke et al. (2019)	all measurements on Kekerengu fault
Ridgecrest 6.4	2019	All	65	0.44	0.34	0.78	18	6.4	3.6	59%	image correlation	Gold et al. (2021)	image correlation, all strands
Ridgecrest 7.1	2019	All	177	1.32	1.02	0.78	50	7.1	3.5	35%	image correlation	Gold et al. (2021)	image correlation, all strands

[a]Full citations are in the reference list.

strike. Parameter values of $D = 0.01$ m^2/year and $K = 0.003$ year^{-1} were used for the hillslope mass transport ('diffusion') coefficient and the water erodibility coefficient, respectively. The parameters controlling incision and diffusion are steady and uniform in each model run, and the fault is simulated as one section of a longer fault to avoid the effects of fault tips. Each model ran for 10 kyr and simulated 2–15 characteristic-slip earthquakes with uniform slip along the fault. A background uplift rate relative to base level of 0.001 m/year was used to maintain a gradient across the model domain. See Duvall and Tucker (2015) and Reitman et al. (2019b) for governing equations and a complete model description.

Here, we test how apparent spatial variability in offset geomorphic markers is affected by fault zone width, length of the earthquake recurrence interval, temporal variability of the recurrence interval, and cumulative slip relative to channel spacing by calculating the $CV_{slip\text{-}spatial}$ [Equation (1)] of all offset measurements from each model run. We also explore how landscape evolution after an earthquake alters the geomorphology of the fault zone. We use the offset distances reported by Reitman et al. (2019b) that were measured at the end of each model run with an automated method that simulates manual interpretation and measurement. We also measure offset markers by hand immediately after each earthquake from an example simulation with five earthquakes of 6 m slip, no distributed deformation, and a 2000-year recurrence interval (Figure 4b).

To compare the accuracy of manual feature interpretation versus automated image correlation, we measure offset distances and track geomorphic change with image correlation. We show an example simulation with five earthquakes of 6 m slip and measure change in modelled topography before and after the first earthquake and in the 1000 years following that earthquake (Figures 6 and 7). Horizontal change is computed with MicMac (Rosu et al., 2015) applied to the post-earthquake topography compared to the pre-earthquake topography and a 9 × 9 pixel correlation window size. Vertical change is calculated by backslipping the post-earthquake topography by the imposed slip amount (6 m) and subtracting the pre-earthquake topography from the backslipped post-earthquake topography. Lateral displacement across the fault is then calculated in 10 m-wide swaths centred every metre along the fault to get a slip distribution along the length of the fault. Linear regressions fit to the data on either side of the fault and projected into the fault zone constrain the magnitude of displacement (e.g. Gold et al., 2015; Milliner et al., 2016a). The regressions are projected 10 m away from the fault to avoid the noise around the fault zone, which is due to the window size of the correlation algorithm and geomorphic change in the fault zone.

3 | RESULTS

Here we present observed variability from the compilation of slip distributions from recent and historical strike-slip earthquakes, then divide the types of contributing variability into introduced and inherent to quantify their relative contributions to total surface slip variability.

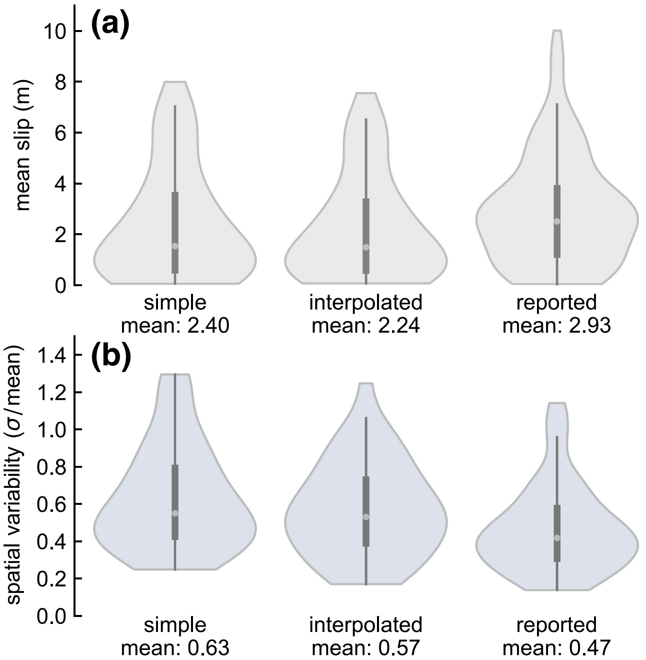

FIGURE 2 Comparison of (a) mean offset value and (b) spatial variability calculated from the mean of all offset measurements (simple), the mean offset value calculated from an interpolated slip distribution sampled at regular intervals (interpolated), and the average offset value reported by the authors (reported). The distributions of mean slip are not significantly different at the 95% confidence level (*t*-test, *p* values range from 0.100 to 0.728). Spatial variability calculated from the reported mean is significantly different from the simple or interpolated methods (95% confidence, *t*-test, $p = 0.002$ and 0.028, respectively) [Color figure can be viewed at wileyonlinelibrary.com]

3.1 | Variability of recent surface ruptures

Surface slip distributions from recent and historical earthquakes have a wide range of spatial variabilities. The average spatial variability of 137 slip distributions from 63 earthquakes is 0.47, with a total range of 0.14–1.14 and an interquartile range of 0.31–0.58 (Figure 3a). The large range of $CV_{slip\text{-}spatial}$ values demonstrates that there is not a typical value of spatial variability for strike-slip faults. The mean spatial variability for single fault section datapoints is 0.43 (Figure 3b) and for multiple fault section datapoints is 0.50 (Figure 3c). These datasets are statistically indistinguishable at the 95% confidence level (*t*-test, $p = 0.45$), suggesting that author-defined fault sections may not provide meaningful subdivisions. The mean spatial variability for subset datapoints is 0.29 (Figure 3d) and for non-subset datapoints is 0.52 (Figure 3e). These two datasets are significantly different at the 95% confidence level (*t*-test, $p \approx 0.00$). The significantly lower variability of subset datasets suggests that interpreting a slip distribution for the most recent earthquake from a dataset that includes larger offsets formed in multiple earthquakes does not accurately represent slip in the last earthquake. These interpreted slip distributions underestimate maximum slip because the largest offsets are interpreted to be formed in multiple prior earthquakes.

The values of spatial variability for non-subset slip distributions reported here are slightly lower than those reported by Lin et al. (2020), because we compute spatial variability using the mean offset value reported by the authors of the study. The mean offset values are not significantly different when calculated from the simple and reported methods, but the reported mean is slightly higher, causing spatial variability to be slightly reduced (Figure 2).

To investigate if spatial variability correlates with rupture characteristics, we compare spatial variability to earthquake magnitude, mean offset, rupture length, and maximum offset for each earthquake, as well as

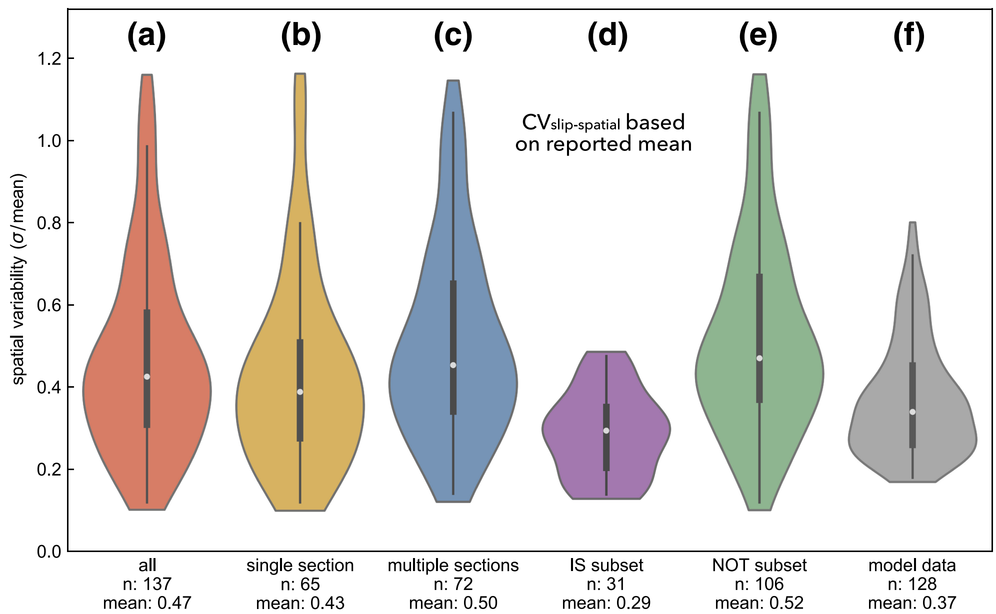

FIGURE 3 Spatial variability of offset measurements from 63 earthquakes calculated using the reported mean offset. The width of each violin is scaled based on the number of datapoints. White circles are median values, and the inner thick bar shows the interquartile range: (a) all data; (b, c) data from single (b) and multiple (c) fault sections, as defined by the authors of the study. (b) and (c) are statistically indistinguishable at the 95% confidence level (*t*-test, $p = 0.45$). (d) Offset measurements subset from a dataset that includes multiple earthquakes. These slip distributions have been interpreted from the larger dataset to represent the most recent rupture. (e) Offset measurements not subset from a larger dataset. (d) and (e) are significantly different at the 95% confidence level (*t*-test, $p \approx 0.00$). (f) Offset measurements from landscape evolution models of constant slip along the fault. The same data for the simple mean calculation are shown in Figure S1 [Color figure can be viewed at wileyonlinelibrary.com]

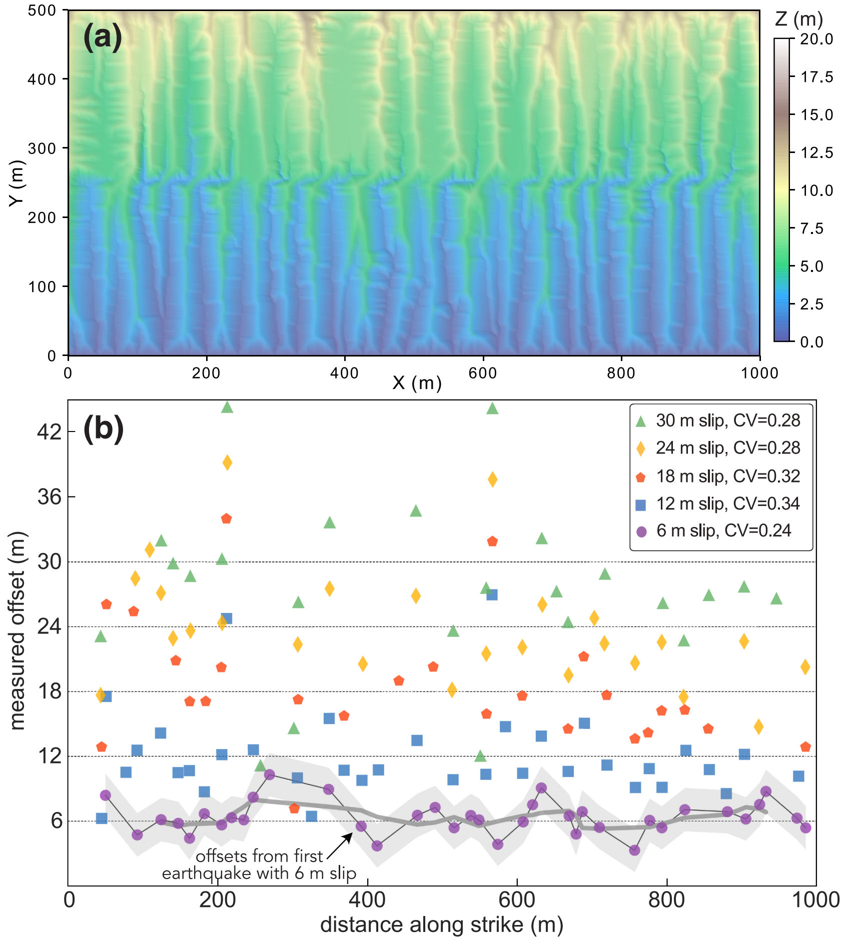

FIGURE 4 Example numerical landscape evolution model output. This model was run for 10 kyr with one 6 m-slip earthquake every 2000 years. (a) Map-view topography at the end of the model run. Offset distances of channels and ridges were mapped and measured following each earthquake, with data shown in (b). Slip distribution (thin black line) and smoothed slip distribution (thick grey line) are shown for the first earthquake with 6 m of slip. Data from Reitman et al. (2019b) [Color figure can be viewed at wileyonlinelibrary.com]

the number of measurements and measurement density for each slip distribution (Figure 8). For spatial variability calculated from the reported mean, there is no apparent correlation with the number of measurements (Figure 8a) or measurement density (Figure 8d). The lack of a trend between the number and variability of measurements suggests that measurement density does not affect the variability calculation.

There is a weak negative correlation between spatial variability and earthquake magnitude ($r^2 = 0.31$; Figure 8). This trend should be considered in context. Mean offset is in the denominator of the $CV_{slip\text{-}spatial}$ equation [Equation (1)]. Earthquakes with larger average slip may seem less variable because there is a minimum threshold on geologists' ability to precisely measure offset in the field and on digital gridded data that depends on the expression of offset in the landscape and the pixel size of the dataset (often 0.5–1.0 m). Smaller earthquakes are more likely to have larger uncertainty relative to mean offset value, which may cause larger spatial variability. The mean offset value usually correlates with rupture length, maximum offset, and earthquake magnitude (e.g. Wells & Coppersmith, 1994), which may explain the slight trend between these characteristics and lower spatial variability.

In summary, we find that no typical variability exists for slip distributions from a single earthquake, and slip distributions derived from larger datasets are less variable than those of recent ruptures. Though larger earthquakes tend to be less variable, this may be a result of a minimum threshold for accurate measurement. In the following two sections, we interrogate the causes and relative contributions of the introduced and inherent variability that comprise the total variability in measured slip distributions.

3.2 | Sources of introduced variability

Introduced surface slip variability is caused by uncertainty in interpretation and measurement. We estimate it in two ways: from modelled offsets and from slip in recent earthquakes measured both by geologists and with image correlation. Apparent spatial variability of offsets from all landscape evolution simulations averages 0.37, with an interquartile range of 0.26–0.45 (Figures 3f and 5). Increased spatial variability correlates with wider fault zones (more distributed deformation, Figures 5a and b), more elapsed time between the earthquake and measuring offset markers (Figures 5c and d), and total slip larger than the distance between channels (Figures 5e and f). The variability of the five populations of offsets measured after each earthquake in the example simulation ranges from 0.24 to 0.34, with a mean value of 0.29 (Figure 4b). Since all modelled earthquakes have constant slip along the fault, these variability values provide an estimate of variability introduced by interpretation and measurement of ∼25–40%.

Image correlation analysis of model output accurately records the imposed lateral slip and supports the estimate of introduced variability. Within 1 year after the earthquake, horizontal image correlation records the imposed 6 m of slip with no spatial variability (Figures 6a and b), whereas the same offset population measured by hand has a $CV_{slip\text{-}spatial}$ of 0.24 (Figure 4b). The high spatial variability of modelled slip when measured by hand compared to the lack of spatial variability when measured with image correlation indicates that interpretation of the fault zone landscape is a large contributor

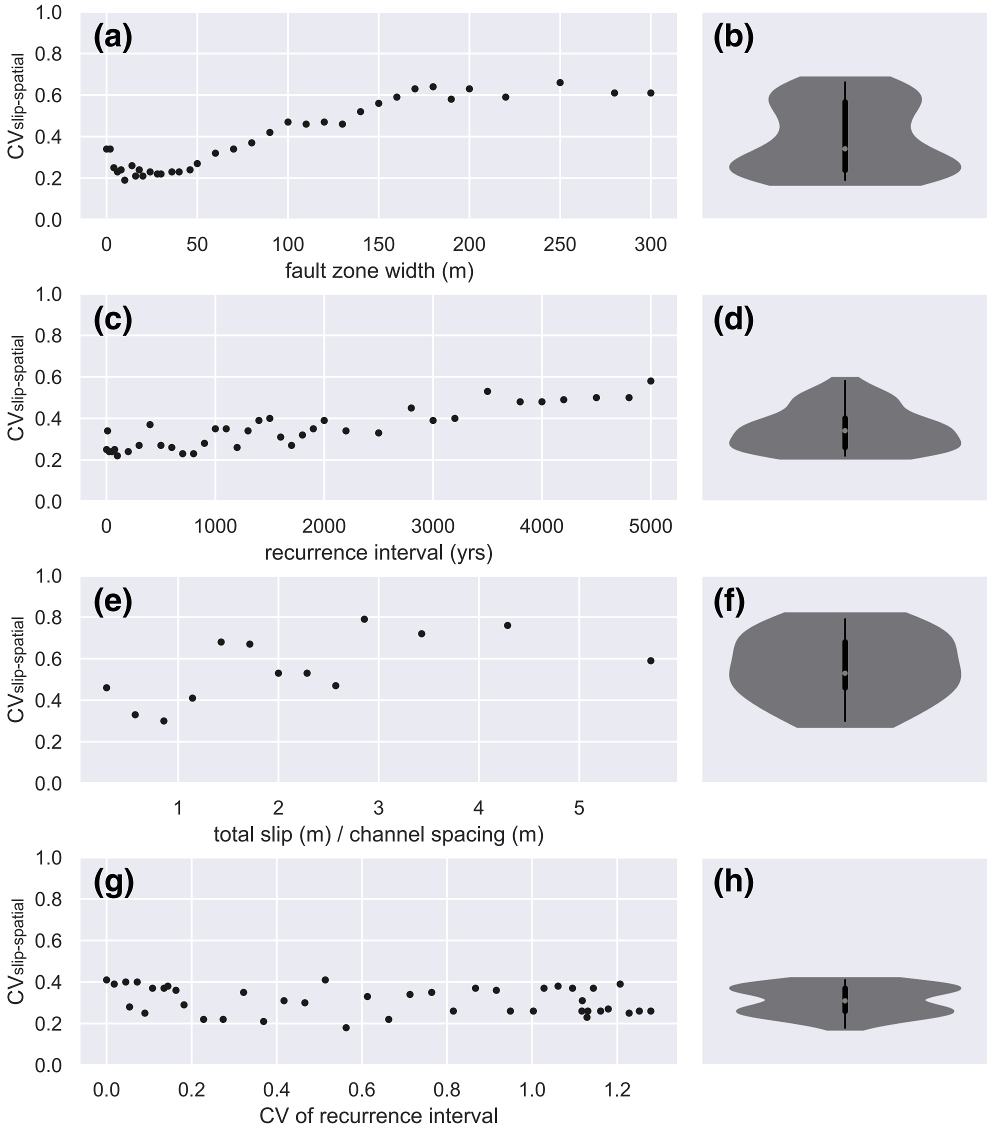

FIGURE 5 Offset measurements from landscape evolution models. Spatial variability was calculated from offset channels measured at the end of each model run for model sets with varying (a, b) fault zone width, (c, d) earthquake recurrence interval, (e, f) channel spacing relative to total slip, and (g, h) temporal variability of the earthquake recurrence interval. Higher spatial variability of offset measurements correlates with wider fault zones, a longer time between earthquake and offset measurement, and total slip larger than channel spacing. Data from Reitman et al. (2019b) [Color figure can be viewed at wileyonlinelibrary.com]

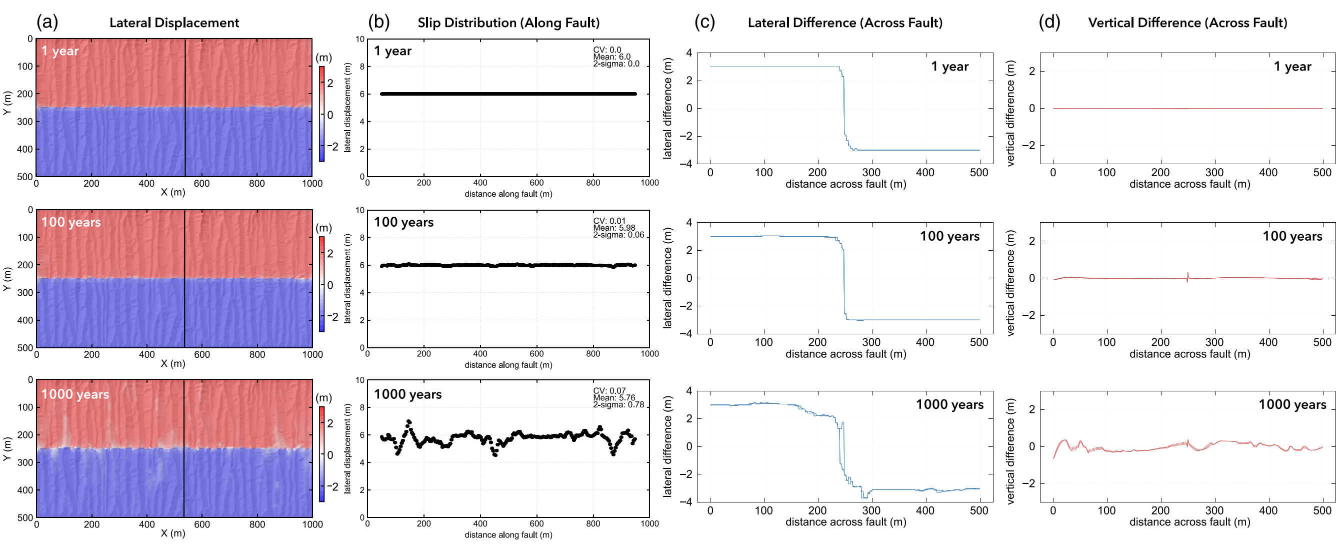

FIGURE 6 Evolution of model topography 1, 100, and 1000 years after an earthquake with 6 m of right-lateral slip. (a) Image correlation results show lateral displacement. Black lines show the location of profiles plotted in (c) and (d). (b) Surface slip distribution derived from image correlation results. (c) Profile across the fault through the image correlation results. (d) Profile across the fault through the vertical differencing results shown in Figure 7. In (c) and (d), the fault is in the centre of each profile (at 250 on the *x*-axis) [Color figure can be viewed at wileyonlinelibrary.com]

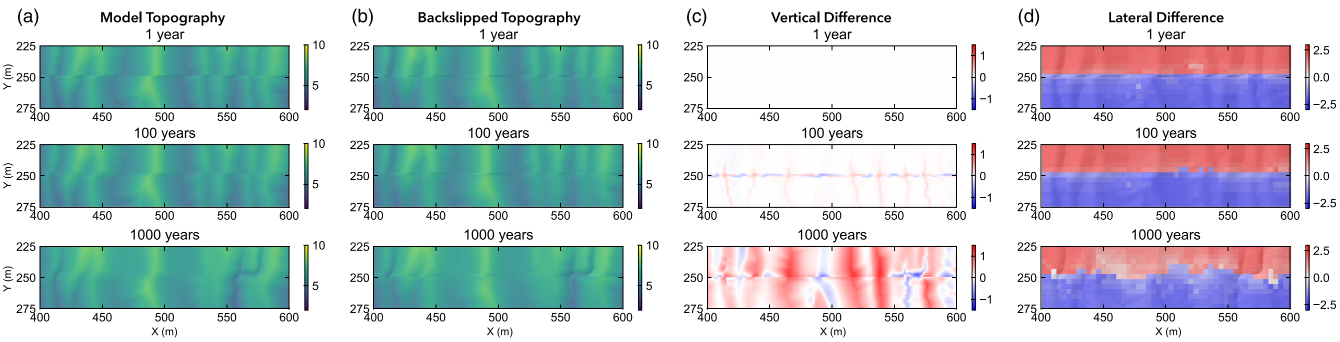

FIGURE 7 Topographic evolution of an example numerical model after an earthquake. (a) Model topography 1, 100, and 1000 years after a 6 m-slip earthquake. (b) The topography in (a) backslipped by 6 m along the fault. (c) Vertical difference between the backslipped topography and pre-earthquake topography. (d) Horizontal difference between the model topography and pre-earthquake topography [Color figure can be viewed at wileyonlinelibrary.com]

to short-wavelength variability in slip distributions measured by hand.

We obtain a second estimate of introduced variability by comparing surface slip measured both by hand and with image correlation in recent ruptures (Figures 9 and 10a). These earthquakes demonstrate a range of short-wavelength variabilities from 0.28 to 0.62 (average 0.42) when measured by hand and 0.09 to 0.29 (average 0.22) when measured with image correlation. In all cases, slip distributions derived from manual measurements are more variable than slip distributions from image correlation. After filtering out long-wavelength variability (grey boxes in Figure 9), slip distributions measured by hand are more variable by 0.10–0.40 (average 0.20) than when measured with image correlation (Figure 9). Although this dataset is small, the range in spatial variability is consistent with estimates of interpretation error from the landscape evolution models.

In summary, we find that slip distributions measured by hand are two times more variable, on average, than slip distributions measured with image correlation and that interpretation and measurement introduce variability of ~25–40%, on average, though variability may be higher or lower in each earthquake.

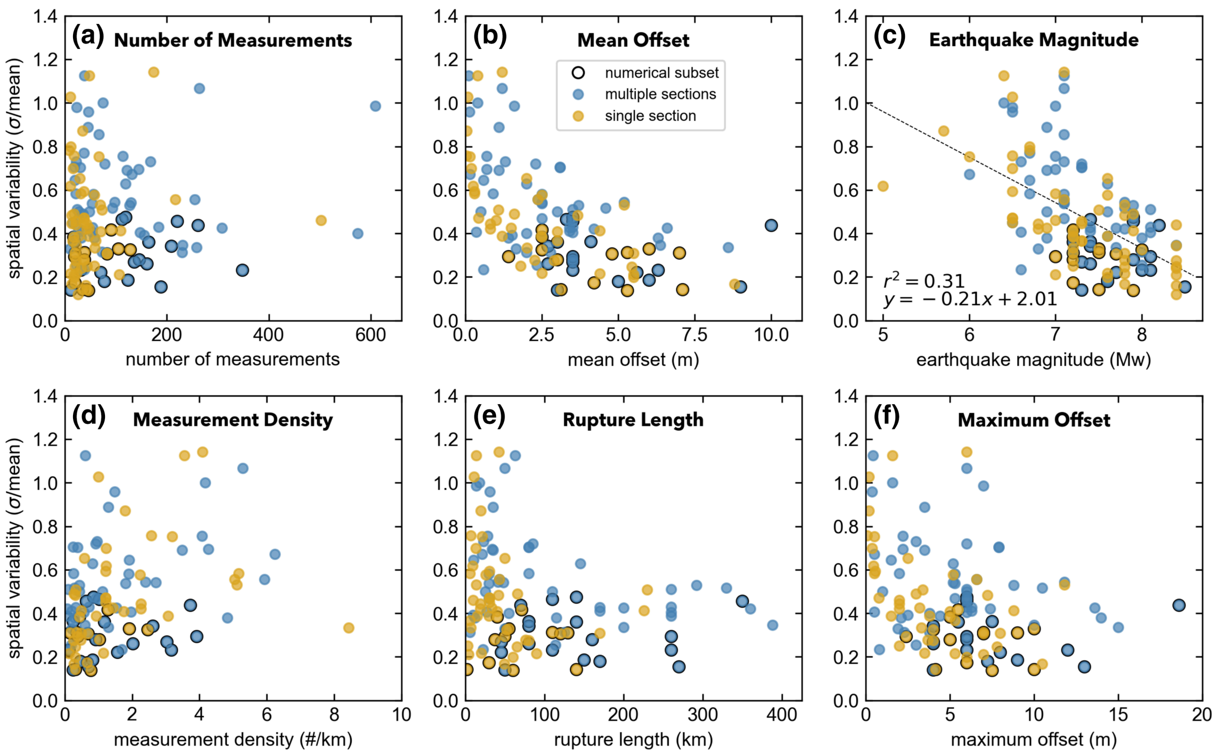

FIGURE 8 Spatial variability of slip distributions from single earthquakes calculated using the reported mean offset as a function of: (a) number of measurements; (b) mean offset; (c) earthquake magnitude; (d) measurement density; (e) rupture length; and (f) maximum offset. Datapoints outlined in black indicate slip distributions interpreted to represent the most recent rupture from a dataset that includes larger offsets from more than one earthquake. Length of the *x*-axis in (d) was clipped to better show clustered datapoints. The same data are shown for spatial variability calculated using the simple mean offset in Figure S2 [Color figure can be viewed at wileyonlinelibrary.com]

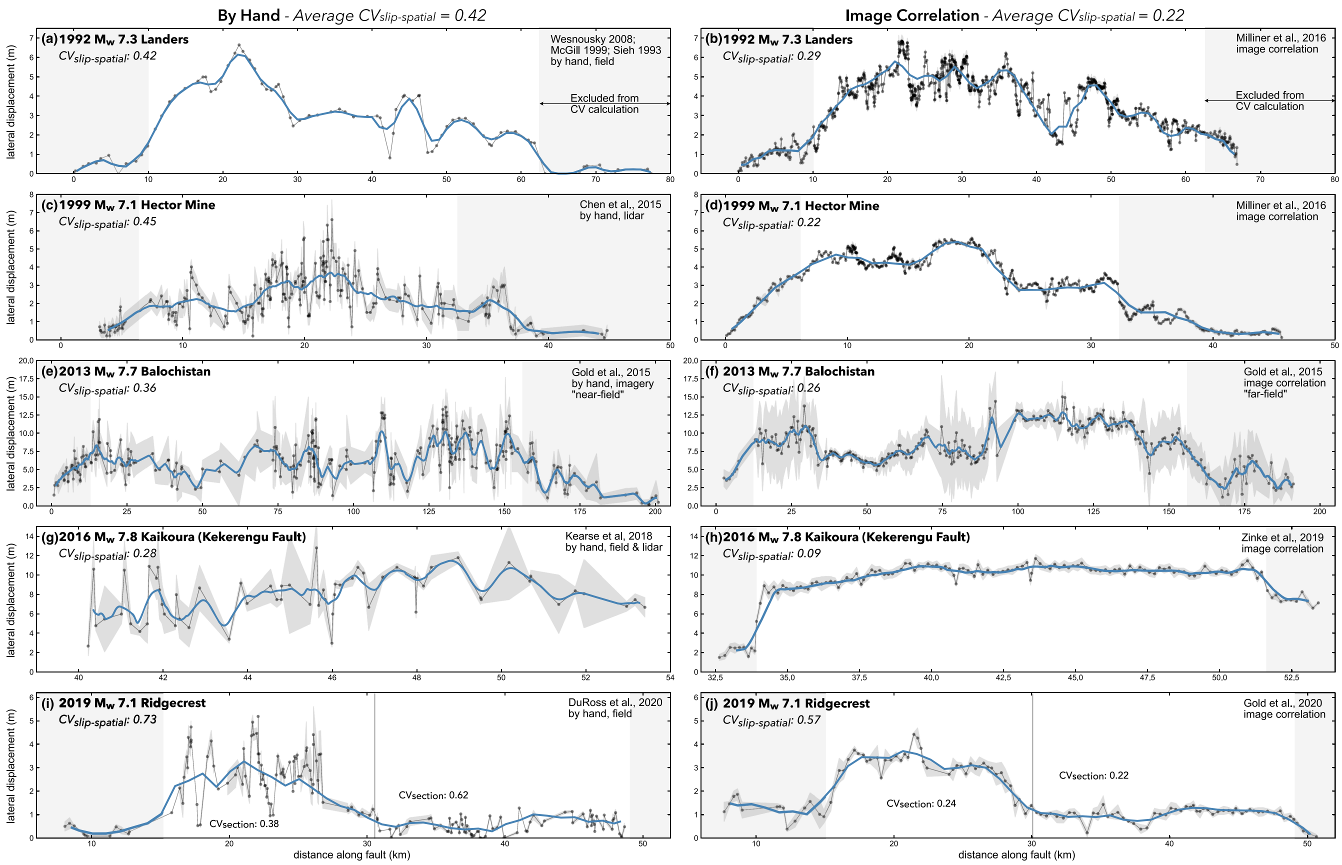

FIGURE 9 Comparison of slip distributions measured by hand and with image correlation for the (a, b) Landers, (c, d) Hector Mine, (e, f) Balochistan, (g, h) Kaikoura, and (i, j) Ridgecrest M_w 7.1 earthquakes. The slip distributions measured by hand are more variable than those measured with image correlation. $CV_{slip\text{-}spatial}$ is shown for the clipped dataset to control for long-wavelength spatial variability. Original data sources shown in each panel. Preferred offsets are shown as circles, with minimum and maximum in the shaded region. Uncertainty values in (b) and (d) are smaller than the marker size for many datapoints. The blue line is a moving average from an interpolated dataset to avoid spatial bias in measurement locations. Grey boxes show data that were clipped to filter out long-wavelength signal [Color figure can be viewed at wileyonlinelibrary.com]

3.3 | Sources of inherent variability

We estimate spatial variability inherent to the rupture process from the seven slip distributions measured with image correlation. Inherent surface slip variability may be caused by multiple fault zone and rupture processes, and we consider the different sources together as an integrated inherent variability. Image correlation analysis integrates the total on-fault and distributed (or 'off-fault') deformation signal, so we consider variability captured by image correlation slip distributions as inherent to surface slip. We assume that additional variability from noise in image correlation is small compared to the magnitude of inherent slip variability, as suggested by the results of applying image correlation to landscape evolution models (Figure 6). Using image correlation on landscape evolution model topography with a known amount of slip, we show that image correlation produces zero variability immediately following an earthquake if linear regressions of profiles are projected across the fault to account for the noise around the fault due to the window size of the correlation algorithm (Figure 6a). This approach is standard practice in real earthquakes (Gold et al., 2015; Milliner et al., 2015; Zinke et al., 2014), suggesting that noise from image correlation is tiny compared to the magnitude of inherent slip variability. In real datasets, the magnitude of noise also depends on the pixel size of the input images, the correlation window size, and processing decisions made by each author. For the studies used in this analysis, image correlation can resolve displacements of 10% or less of the image pixel size (i.e. 10 cm for 1 m-resolution images) and profile stacking is used to further smooth out noise and increase signal-to-noise ratio (Gold et al., 2015, 2021; Milliner et al., 2015, 2016b; Zinke et al., 2014). Synthetic tests also demonstrate that three different correlation algorithms can resolve displacement between 1/10th and 1/100th of the image pixel size with little noise, especially when pixels with low signal-to-noise ratio are masked out (Leprince et al., 2007; Rosu et al., 2015). Therefore, noise in the image correlation datasets is a small fraction of each offset measurement and variability recorded with image correlation on real faults mostly captures the variability inherent to the rupture process.

Spatial variability for the slip distributions measured with image correlation ranges from 0.24 to 0.78, with a mean of 0.53 (Table 2). When long-wavelength variability (grey boxes in Figure 9) is filtered out of the slip distributions to isolate short-wavelength variability, $CV_{slip\text{-}spatial}$ drops to 0.09–0.29, with a mean of 0.22 (Figure 9). The strong positive correlation between spatial variability of slip

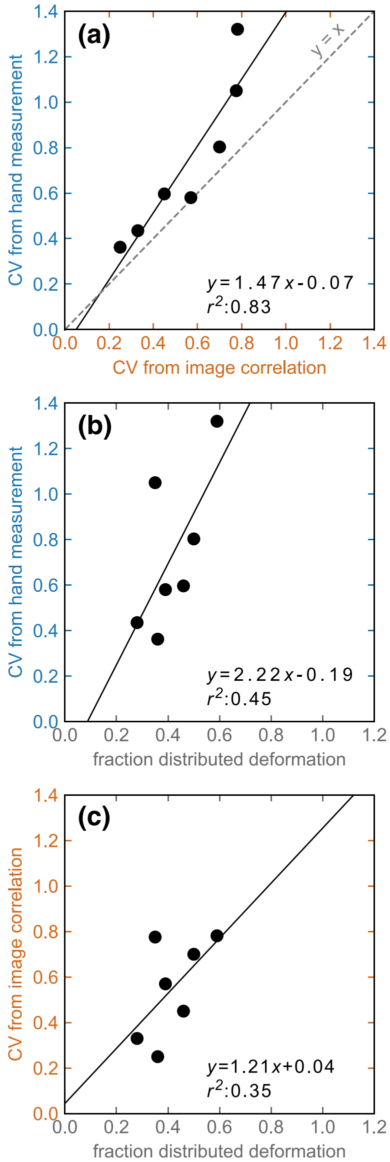

FIGURE 10 Relationship between distributed deformation and spatial variability. (a) There is a strong positive correlation between $CV_{slip\text{-}spatial}$ measured by hand and with image correlation. (b) There is a moderate positive correlation between distributed deformation and spatial variability when measured by hand, and (c) a weaker positive correlation between distributed deformation and spatial variability when measured with image correlation [Color figure can be viewed at wileyonlinelibrary.com]

distributions measured by hand and with image correlation (Figure 10a) also demonstrates that some earthquakes naturally have more variable surface ruptures than others.

4 | DISCUSSION

4.1 | Variability from interpretation and measurement

Interpretation error is the variability introduced by the process of identifying offset features, correlating them across the fault, and reconstructing the offset amount. Measurement error is the random error introduced by measuring an offset marker. Gold et al. (2013) found measurement error of ±11% from single user repeat measurements of offset features from the 2010 El Mayor Cucapah earthquake. In this study we estimate interpretation and measurement error at ∼25–40% based on the numerical models and recent ruptures, though the exact amount of variability may depend on the scientist doing the analysis and their experience level (Salisbury et al., 2015; Scharer et al., 2014). Other studies have also quantified interpretation error. McGill and Rubin (1999) found that offset markers from the 1992 Landers earthquake measured by different groups of researchers range in difference from 0.01 to 1.6 m, with an average difference of 0.5 m. Scharer et al. (2014) report an offset measurement range of 2.6 m for one offset channel measured by nine different field parties. These prior studies support our finding, derived from assessment of landscape evolution models, that interpretation error can be very large and greatly exceeds measurement error.

Interpretation error is larger than measurement error because it relies on correctly identifying characteristics of both the fault and offset marker at each measurement location. The scientist must identify the fault location, fault strike, and fault zone width in the local region of the offset feature, as well as infer the pre-earthquake morphology of the offset marker, the angle of intersection with the fault, and any post-earthquake geomorphic modification. High obliquity, sinuosity, and width of the offset marker make it difficult to interpret pre-earthquake morphology (Salisbury et al., 2015; Scharer et al., 2014; Zielke et al., 2015). The complexity and width of the fault zone also affects accuracy of the projection of the offset marker into the fault zone (e.g. Zielke et al., 2015). Since measurement error can be an order of magnitude lower than interpretation uncertainty (Gold et al., 2013), and sizable differences in offset estimates are more likely to result from improper interpretation than measurement, we suggest that measurement error is accounted for within the reported uncertainty bounds, rather than in addition to the interpretation error. Interpretation error is thus the major source of introduced variability, provoking the question: what causes large interpretation errors?

4.2 | Variability from geomorphic change in the fault zone

Perhaps the largest source of interpretation error is the geomorphic expression of lateral slip in the fault zone. In the landscape evolution model, apparent variability from interpretation error is high after a single earthquake (24%, Figure 4b) and increases with more earthquakes and increased time since an earthquake. Interpretation may become more difficult as slip accumulates on a fault, because of geomorphic evolution due to erosion and deposition in the interseismic period and the expression of cumulative slip in fault zone geomorphology.

Progressive landscape evolution in the interseismic period may increase interpretation error for historical earthquakes. For example, reconstructing the original offset geometry for historical earthquakes becomes more difficult as the preservation of the fault and offset markers degrades due to erosion, deposition, and widening of the geomorphic fault zone (Lienkaemper & Strum, 1989; Noriega et al., 2006; Reitman et al., 2019b; Sharp et al., 1989). Image correlation of numerical models illustrates landscape change after one earthquake (Figures 6 and 7). Horizontal difference results show increasing noise in the fault zone 1, 100, and 1000 years after the earthquake

(Figure 6a) and the corresponding increase in variability of the slip distribution (Figure 6b) and noise in across-fault profiles (Figure 6c). Vertical difference results also illustrate topographic change initiating in the fault zone and channels within 100 years and permeating the model landscape by 1000 years after the earthquake (Figures 6d and 7). In this model setup, the fault zone landscape has changed so much by 1000 years after the earthquake that backslipping the model topography results in a discrete break along the fault (Figures 7b and c), an indication that the original lateral displacement has been smoothed. At this time, the mean offset value slightly underestimates imposed slip, but individual offset measurements both over- and underestimate modelled slip (Figure 6b). The exact timescales of these processes depend on the local climate and the near-surface material in the fault zone, but the models demonstrate how reconstructing offset features provides a less accurate slip distribution for a historical earthquake than for a modern one. The image correlation results highlight landscape change after a single earthquake; interpretation error likely increases when the next earthquake occurs, imprinting fresh surface rupture on the degraded expression of the prior earthquake.

As slip accumulates in multiple earthquakes, new offset channels are created, some offset channels grow longer, and some are erased. These processes also make interpretation more difficult and can increase spatial variability in offset measurements. Two processes can erase or reset an offset channel: channel aliasing and channel avulsion. Channel aliasing occurs when fault slip exceeds the distance between channels and channel heads disconnect from their original tails and capture the tails of neighbouring channels. This process creates an aliasing effect between the upstream and downstream portions of channels that cross a strike-slip fault and has been observed in numerical models (Duvall & Tucker, 2015; Reitman et al., 2019b) and in the Carrizo Plain section of the San Andreas Fault (Noriega et al., 2006; Salisbury et al., 2018). In the numerical models, spatial variability increased as cumulative slip exceeded channel spacing (Figure 5e), because channel aliasing may cause apparent left-lateral offsets in a right-lateral system and offsets appearing smaller or larger than imposed slip.

Another process that erases the initial offset occurs when a strike-slip earthquake changes the gradient in the long profile of an offset channel. Lateral slip can flatten the gradient of the long profile of an offset channel along the fault scarp, which then increases aggradation and eventually may cause the channel to spill over (avulse) and incise a new channel. This process resets the original offset distance and provides a maximum offset amount recorded in a landscape (Dascher-Cousineau et al., 2021; Sims, 1994). These examples illustrate how geomorphic processes can play a primary role in the development and modification of channel offsets, illustrating the intertwined influences of tectonics and climate in shaping a fault zone landscape and highlighting the difficulties in interpreting strike-slip geomorphology.

In summary, landscape evolution during the interseismic period, channel avulsion, and channel aliasing all increase spatial variability of offset marker measurements because they alter the original offset features and impede interpretation. These issues are magnified as time passes after an earthquake, underscoring the importance of measuring offset features quickly and highlighting the difficulties in determining accurate slip distributions for historical earthquakes. How these effects are compounded in multiple earthquakes remains to be tested.

4.3 | Variability from distributed deformation

Some of the difference between hand-measured and image correlation slip distributions from real earthquakes is caused by distributed deformation, slip that is localized on a fault at depth but is distributed up to a few hundred metres around the fault at the surface (sometimes referred to as off-fault deformation). Distributed deformation is common in surface ruptures and is easily missed by near-fault hand measurements. Estimates of distributed deformation for the earthquakes in Table 2 range from 28 to 59%, with an average of 42%, as reported by the authors of each study. For these events, far-field slip measured by image correlation usually exceeds near-field offset measurements made by hand (Figure 9) and is always less variable (Figure 10a), partly because near-field measurements made by hand may not capture the entire deformation field (e.g. Gold et al., 2015; Milliner et al., 2015). There is a moderate positive correlation between spatial variability and distributed deformation for the slip distributions measured by hand (Figure 10b). This correlation may exist because it is more difficult to recognize and measure distributed deformation in the field than discrete, brittle failure that occurs on a fault. McGill and Rubin (1999) proposed that short-wavelength spatial variability in the 1992 Landers slip distribution was due to incomplete expression of slip at the fault because of distributed brittle shear, warping, or small block rotations. Similarly, variability of offset measurements increased with wider fault zones in the landscape evolution models (Figure 5a). The weaker positive correlation between distributed deformation and slip distributions measured with image correlation (Figure 10c) suggests that missing distributed deformation explains some, but not all, of the spatial variability in slip distributions measured by hand.

Distributed deformation is inherent to the rupture process, but its root cause and why it is spatially variable remain open questions. Hypotheses for the cause of distributed deformation largely overlap with the potential causes of inherent slip variability, for example: strength of near-surface materials or inelastic strain. Both McGill and Rubin (1999) and Milliner et al. (2015) found a weak inverse correlation between the strength of near-surface material and the amount of distributed deformation for the 1992 Landers earthquake. Zinke et al. (2014) also suggested that the strength of surficial material correlates with distributed deformation for the 2013 Balochistan earthquake, and Cheng and Barnhart (2021) found no correlation between distributed deformation and inelastic strain in this rupture. Because distributed deformation is likely an integral of multiple causes, fault maturity, fault strength, and slip in prior earthquakes may also play a role. It also remains unknown if the pattern of distributed deformation is constant or variable in successive earthquakes. Because distributed deformation is generally not preserved in the landscape long after an earthquake, there aren't any data to answer these questions, and slip distributions for historical earthquakes underestimate the total deformation field.

In summary, distributed deformation accounts for some of the spatial variability in slip distributions measured by hand, and it is not captured in the hand-measured, near-fault geomorphic record of lateral displacement. These results suggest caution in interpreting offset geomorphic markers from historical and paleoseismic earthquakes to infer slip-per-event and slip distribution of prior earthquakes. Estimates of slip distribution in prehistoric earthquakes derived primarily from geomorphic features likely underestimate maximum slip because they miss distributed deformation and may attribute large offsets to older earthquakes.

5 | CONCLUSION

Observed short-wavelength spatial variability in surface slip along strike-slip faults is due to both interpretation error and inherent variability, possibly in equal measure or dominated by introduced variability. The relative contribution of the two sources likely varies between different fault sections and earthquakes. Apparent spatial variability introduced by interpretation of the landscape contributes ~25–40% variability for simple strike-slip faults simulated in numerical landscape evolution models with constant slip along the fault. Short-wavelength variability inherent to the rupture process ranges from 9 to 29%, as constrained by seven recent surface ruptures measured with image correlation. Distributed deformation, landscape evolution via erosion and deposition in the interseismic period, and channel aliasing make interpretation of the landscape more difficult and contribute to variability in slip distributions measured by hand. Though there is no typical value of spatial variability, slip distributions derived from larger datasets that include offsets from multiple earthquakes are significantly less variable than slip distributions from recent ruptures. These results suggest that inherent variability in slip distributions and the variability introduced by human interpretation combine to yield estimates that systematically underestimate maximum surface slip in historical earthquakes.

ACKNOWLEDGEMENTS

This material is based on work supported by the National Science Foundation Graduate Research Fellowship Program under Grant No. DGE-1650115 to NR. Landlab is an element of the Community Surface Dynamics Modeling System (CSDMS), which is supported by the US National Science Foundation (EAR-1831623). The free Tabula and WebPlotDigitizer programs made the data compilation possible. Conversations with Ryan Gold, Rich Briggs, Craig Jones, and Peter Molnar were incredibly valuable in shaping this study. Thanks to Rich Briggs for reading a draft and to two anonymous reviewers for their constructive reviews.

AUTHOR CONTRIBUTIONS

NR: (a) conceptualization, (b) funding acquisition, (c) methodology, (d) investigation, (f) software, (h) writing—initial draft, (i) writing—reviewing and editing.

GT: (c) methodology, (f) software, (g) supervision, (i) writing—reviewing and editing.

KM: (a) conceptualization, (e) resources, (g) supervision, (i) writing—reviewing and editing.

DATA AVAILABILITY STATEMENT

This study used data from Reitman et al. (2019a) available at DOI: 10.5281/zenodo.3374026. Data from Baize et al. (2019), Lin et al. (2020), and Wesnousky (2008) are available in the supplements to their papers. All slip distributions were taken from published papers. All data generated by this study are included as tables.

ORCID

Nadine G. Reitman https://orcid.org/0000-0002-6730-2682
Gregory E. Tucker https://orcid.org/0000-0003-0364-5800

REFERENCES

Akyüz, H.S., Hartleb, R., Barka, A., Altunel, E., Sunal, G., Meyer, B. & Armijo, R. (2002) Surface rupture and slip distribution of the 12 November 1999 Düzce earthquake (M 7.1), North Anatolian fault, Bolu, Turkey. *Bulletin of the Seismological Society of America*, 92(1), 61–66. https://doi.org/10.1785/0120000840

Ansberque, C., Bellier, O., Godard, V., Lasserre, C., Wang, M., Braucher, R., *et al*. (2016) The Longriqu fault zone, eastern Tibetan Plateau. *Segmentation and Holocene Behavior: Tectonics*, 35(3), 565–585. https://doi.org/10.1002/2015TC004070

Awata, Y., Mizuno, K., Sugiyama, Y., Imura, R., Shimokawa, K., Okumura, K. & Tsukuda, E. (1996) Surface fault ruptures on the northwest coast of Awaji Island associated with the Hyogo-ken Nanbu earthquake of 1995, Japan. *Journal of the Seismological Society of Japan*, 2(1), 113–124. https://doi.org/10.4294/zisin1948.49.1_113

Baize, S., Nurminen, F., Sarmiento, A., Dawson, T., Takao, M., Scotti, O., *et al*. (2019) A worldwide and unified database of surface ruptures (SURE) for fault displacement hazard analyses. *Seismological Research Letters*, 91(1), 499–520. https://doi.org/10.1785/0220190144

Barka, A. (1996) Slip distribution along the North Anatolian fault associated with the large earthquakes of the period 1939 to 1967. *Bulletin of the Seismological Society of America*, 86, 1238–1254. https://doi.org/10.1785/BSSA0860051238

Barka, A., Akyüz, H.S., Altunel, E., Sunal, G., Çakir, Z., Dikbas, A., *et al*. (2002) The surface rupture and slip distribution of the 17 August 1999 İzmit earthquake (M 7.4), North Anatolian fault. *Bulletin of the Seismological Society of America*, 92(1), 43–60. https://doi.org/10.1785/0120000841

Barnhart, K.R., Hutton, E.W.H., Tucker, G.E., Gasparini, N.M., Istanbulluoglu, E., Hobley, D.E.J., *et al*. (2020a) Short communication: Landlab v2.0: A software package for Earth surface dynamics. *Earth Surface Dynamics*, 8(2), 379–397. https://doi.org/10.5194/esurf-8-379-2020

Barnhart, W.D., Gold, R.D. & Hollingsworth, J. (2020b) Localized fault-zone dilatancy and surface inelasticity of the 2019 Ridgecrest earthquakes. *Nature Geoscience*, 13(10), 699–704. https://doi.org/10.1038/s41561-020-0628-8

Berberian, M., Asudeh, I. & Arshadi, S. (1979) Surface rupture and mechanism of the Bob-Tangol (southeastern Iran) earthquake of 19 December 1977. *Earth and Planetary Science Letters*, 42(3), 456–462. https://doi.org/10.1016/0012-821X(79)90055-4

Berberian, M., Jackson, J.A., Ghorashi, M. & Kadjar, M.H. (1984) Field and teleseismic observations of the 1981 Golbaf–Sirch earthquakes in SE Iran. *Geophysical Journal of the Royal Astronomical Society*, 77(3), 809–838. https://doi.org/10.1111/j.1365-246X.1984.tb02223.x

Berberian, M., Jackson, J.A., Qorashi, M., Khatib, M.M., Priestley, K., Talebian, M. & Ghafuri-Ashtiani, M. (1999) The 1997 May 10 Zirkuh (Qa'enat) earthquake (M[w] 7.2): Faulting along the Sistan suture zone of eastern Iran. *Geophysical Journal International*, 136, 671–694. https://doi.org/10.1046/j.1365-246X.1999.00762.x

Berberian, M., Jackson, J.A., Fielding, E., Parsons, B.E., Priestley, K., Qorashi, M., *et al*. (2001) The 1998 March 14 Fandoqa earthquake (M_w 6.6) in Kerman Province, southeast Iran: Re-rupture of the 1981 Sirch earthquake fault, triggering of slip on adjacent thrusts and the active tectonics of the Gowk fault zone. *Geophysical Journal International*, 146(2), 371–398. https://doi.org/10.1046/j.1365-246X.2001.01459.x

Bi, H., Zheng, W., Lei, Q., Zeng, J., Zhang, P. & Chen, G. (2020) Surface slip distribution along the West Helanshan Fault, Northern China, and its implications for fault behavior. *Journal of Geophysical Research: Solid Earth*, 125(7), 1–20. https://doi.org/10.1029/2020JB019983

Brooks, B.A., Minson, S.E., Glennie, C.L., Nevitt, J.M., Dawson, T., Rubin, R., *et al*. (2017) Buried shallow fault slip from the South Napa earthquake revealed by near-field geodesy. *Science Advances*, 3(7), 1–12. https://doi.org/10.1126/sciadv.1700525

Bruhat, L., Klinger, Y., Vallage, A. & Dunham, E.M. (2019) Influence of fault roughness on surface displacement: From numerical simulations to coseismic slip distributions. *Geophysical Journal International*, 220(3), 1857–1877. https://doi.org/10.31223/OSF.IO/CNKSH

Champenois, J., Baize, S., Vallee, M., Jomard, H., Alvarado, A., Espin, P., *et al*. (2017) Evidences of surface rupture associated with a low-magnitude (M_w 5.0) shallow earthquake in the Ecuadorian Andes. *Journal of Geophysical Research: Solid Earth*, 122(10), 8446–8458. https://doi.org/10.1002/2017JB013928

Chen, T., Akciz, S.O., Hudnut, K.W., Zhang, D.Z. & Stock, J.M. (2015) Fault-slip distribution of the 1999 M_w 7.1 Hector Mine earthquake, California, estimated from postearthquake airborne LiDAR data. *Bulletin of the Seismological Society of America*, 105(2A), 776–790. https://doi.org/10.1785/0120130108

Chen, T., Liu-Zeng, J., Shao, Y., Zhang, P., Oskin, M.E., Lei, Q. & Li, Z. (2018) Geomorphic offsets along the creeping Laohu Shan section of the Haiyuan fault, northern Tibetan Plateau. *Geosphere*, 14(3), 1165–1186. https://doi.org/10.1130/GES01561.1

Cheng, G. & Barnhart, W.D. (2021) Permanent co-seismic deformation of the 2013 M_w 7.7 Baluchistan, Pakistan earthquake from high-resolution surface strain analysis. *Journal of Geophysical Research: Solid Earth*, 126(3), 1–19. https://doi.org/10.1029/2020JB020622

Choi, J.-H.H., Jin, K., Enkhbayar, D., Davvasambuu, B., Bayasgalan, A. & Kim, Y.S. (2012) Rupture propagation inferred from damage patterns, slip distribution, and segmentation of the 1957 M_w 8.1 Gobi-Altay earthquake rupture along the Bogd fault, Mongolia. *Journal of Geophysical Research*, 117(B12), 1–24. https://doi.org/10.1029/2011JB008676

Choi, J.-H.H., Klinger, Y., Ferry, M., Ritz, J.-F.F., Kurtz, R., Rizza, M., *et al*. (2018) Geologic inheritance and earthquake rupture processes: The 1905 M ≥ 8 Tsetserleg-Bulnay strike-slip earthquake sequence, Mongolia. *Journal of Geophysical Research: Solid Earth*, 123(2), 1925–1953. https://doi.org/10.1002/2017JB013962

Clark, M.M. (1972) Surface rupture along the Coyote Creek fault: U.S. Geological Survey Professional Paper: The Borrego Mountain Earthquake of April 9, 1968, v. 207, p. 55–86.

Dascher-Cousineau, K., Finnegan, N.J. & Brodsky, E.E. (2021) The life span of fault-crossing channels. *Science*, 373(6551), 204–207. https://doi.org/10.1126/science.abf2320

DuRoss, C.B., Gold, R.D., Dawson, T.E., Scharer, K.M., Kendrick, K.J., Akciz, S.O., *et al*. (2020) Surface displacement distributions for the July 2019 Ridgecrest, California, earthquake ruptures. *Bulletin of the Seismological Society of America*, 110(4), 1400–1418. https://doi.org/10.1785/0120200058

Duvall, A.R. & Tucker, G.E. (2015) Dynamic ridges and valleys in a strike-slip environment. *Journal of Geophysical Research – Earth Surface*, 120(10), 2016–2026. https://doi.org/10.1002/2015JF003618

Elliott, J.R., Nissen, E.K., England, P.C., Jackson, J.A., Lamb, S., Li, Z. & Oehlers, M. (2012) Slip in the 2010–2011 Canterbury earthquakes, New Zealand. *Journal of Geophysical Research: Solid Earth*, 117(B3), B03401. https://doi.org/10.1029/2011JB008868

Elliott, A.J., Oskin, M.E., Liu-Zeng, J. & Shao, Y. (2015) Rupture termination at restraining bends: The last great earthquake on the Altyn Tagh Fault. *Geophysical Research Letters*, 42(7), 2164–2170. https://doi.org/10.1002/2015GL063107

Emre, Ö., Kondo, H., Özalp, S. & Elmacı, H. (2020) Fault geometry, segmentation and slip distribution associated with the 1939 Erzincan earthquake rupture along the North Anatolian fault, Turkey: SP501–2019-141, 501, 23, 70.

Fletcher, J.M., Teran, O.J., Rockwell, T.K., Oskin, M.E., Hudnut, K.W., Mueller, K.J., *et al*. (2014) Assembly of a large earthquake from a complex fault system: Surface rupture kinematics of the 4 April 2010 El Mayor-Cucapah (Mexico) M_w 7.2 earthquake. *Geosphere*, 10, 797–827. https://doi.org/10.1130/GES00933.1

Fukuyama, E., Muramatu, I. & Mikumo, T. (2007) Seismic moment of the 1891 Nobi, Japan, earthquake estimated from historical seismograms. *Earth, Planets and Space*, 59(6), 553–559. https://doi.org/10.1186/BF03352717

Gold, P.O., Oskin, M.E., Elliott, A.J., Hinojosa-Corona, A., Taylor, M.H., Kreylos, O. & Cowgill, E. (2013) Coseismic slip variation assessed from terrestrial LiDAR scans of the El Mayor–Cucapah surface rupture. *Earth and Planetary Science Letters*, 366, 151–162. https://doi.org/10.1016/j.epsl.2013.01.040

Gold, R.D., Reitman, N.G., Briggs, R.W., Barnhart, W.D., Hayes, G.P. & Wilson, E. (2015) On- and off-fault deformation associated with the September 2013 M_w 7.7 Balochistan earthquake: Implications for geologic slip rate measurements. *Tectonophysics*, 660, 65–78. https://doi.org/10.1016/j.tecto.2015.08.019

Gold, R.D., DuRoss, C.B. & Barnhart, W.D. (2021) Coseismic surface displacement in the 2019 Ridgecrest earthquakes: Comparison of field measurements and optical image correlation results. *Geochemistry, Geophysics, Geosystems*, 22(3), e2020GC009326. https://doi.org/10.1029/2020GC009326

Guo, P., Han, Z., Dong, S., Yuan, R. & Xie, Z. (2019) Surface rupture and slip distribution along the Lenglongling fault in the NE Tibetan Plateau: Implications for faulting behavior. *Journal of Asian Earth Sciences*, 172, 190–207. https://doi.org/10.1016/j.jseaes.2018.09.008

Haddon, E.K., Amos, C.B., Zielke, O., Jayko, A.S. & Burgmann, R. (2016) Surface slip during large Owens Valley earthquakes. *Geochemistry, Geophysics, Geosystems*, 17(6), 2239–2269. https://doi.org/10.1002/2015GC006033

Haeussler, P.J., Schwartz, D.P., Dawson, T., Stenner, H., Lienkaemper, J., Sherrod, B., *et al*. (2004a) Surface rupture and slip distribution of the Denali and Totschunda faults in the 3 November 2002 M 7.9 earthquake, Alaska. *Bulletin of the Seismological Society of America*, 94(6B), S23–S52. https://doi.org/10.1785/0120040626

Haeussler, P.J., Schwartz, D.P., Dawson, T.E., Stenner, H.D., Lienkaemper, J.J., Cinti, F.R., *et al*. (2004b) Surface rupture of the 2002 Denali fault, Alaska, earthquake and comparison with other strike-slip ruptures. *Earthquake Spectra*, 20(3), 565–578. https://doi.org/10.1193/1.1775797

Han, N., Shan, X., Song, X., Ren, Z., Gong, W. & Wang, Z. (2018) Paleoseismic study on the Pingdingshan-Annanba segments of the Altyn Tagh Fault based on offset clusters. *Journal of Structural Geology*, 115, 19–27. https://doi.org/10.1016/j.jsg.2018.06.020

Han, S., Li, H., Pan, J., Lu, H., Zheng, Y., Liu, D. & Ge, C. (2019) Co-seismic surface ruptures in Qiangtang Terrane: Insight into Late Cenozoic deformation of central Tibet. *Tectonophysics*, 750, 359–378. https://doi.org/10.1016/j.tecto.2018.11.001

Hobley, D.E.J., Adams, J.M., Siddhartha Nudurupati, S., Hutton, E.W.H., Gasparini, N.M., Istanbulluoglu, E. & Tucker, G.E. (2017) Creative computing with Landlab: An open-source toolkit for building, coupling, and exploring two-dimensional numerical models of Earth-surface dynamics. *Earth Surface Dynamics*, 5(1), 21–46. https://doi.org/10.5194/esurf-5-21-2017

Jiang, W., Zhang, J., Han, Z., Tian, T., Jiao, Q., Wang, X. & Jiang, H. (2017) Characteristic slip of strong earthquakes along the Yishu Fault Zone in East China evidenced by offset landforms. *Tectonics*, 36(10), 1947–1965. https://doi.org/10.1002/2016TC004363

Kang, W., Xu, X., Oskin, M.E., Yu, G., Luo, J., Chen, G., *et al*. (2020) Characteristic slip distribution and earthquake recurrence along the eastern Altyn Tagh fault revealed by high-resolution topographic data. *Geosphere*, 16(1), 392–406. https://doi.org/10.1130/GES02116.1

Kearse, J., Little, T.A., van Dissen, R.J., Barnes, P.M., Langridge, R., Mountjoy, J., *et al*. (2018) Onshore to offshore ground-surface and seabed rupture of the Jordan–Kekerengu–Needles fault network during the 2016 M_w 7.8 Kaikōura earthquake, New Zealand. *Bulletin of the Seismological Society of America*, 108(3B), 1573–1595. https://doi.org/10.1785/0120170304

Klinger, Y., Xu, X., Tapponnier, P., Lasserre, C., King, G., Van der Woerd, J. J., *et al*. (2005) High-resolution satellite imagery mapping for the surface rupture and slip distribution of the M_w ~7.8, 14 November 2001 Kokoxili earthquake, Kunlun fault, northern Tibet, China. *Bulletin of the Seismological Society of America*, 95(5), 1970–1987. https://doi.org/10.1785/0120040233

Klinger, Y., Etchebes, M., Tapponnier, P. & Narteau, C. (2011) Characteristic slip for five great earthquakes along the Fuyun fault in China. *Nature Geoscience*, 4(6), 389–392. https://doi.org/10.1038/ngeo1158

Kondo, H., Awata, Y., Emre, O., Dogan, A., Ozalp, S., Tokay, F., *et al*. (2005) Slip distribution, fault geometry, and fault segmentation of the 1944

Bolu-Gerede earthquake rupture, North Anatolian Fault, Turkey. *Bulletin of the Seismological Society of America*, 95(4), 1234–1249. https://doi.org/10.1785/0120040194

Kurtz, R., Klinger, Y., Ferry, M. & Ritz, J.-F. (2018) Horizontal surface-slip distribution through several seismic cycles: The Eastern Bogd fault, Gobi-Altai, Mongolia. *Tectonophysics*, 734–735, 167–182. https://doi.org/10.1016/j.tecto.2018.03.011

Kurushin, R.A., Bayasgalan, A., Ölziybat, M., Enhtuvshin, B., Molnar, P., Bayarsayhan, C., *et al*. (1997) The surface rupture of the 1957 Gobi-Altay, Mongolia, earthquake: Boulder, Colorado. *Geological Society of America Special Paper*, 320, 1–144. https://doi.org/10.1130/0-8137-2320-5.1

Leprince, S., Barbot, S., Ayoub, F. & Avouac, J.-P. (2007) Automatic and precise orthorectification, coregistration, and subpixel correlation of satellite images, application to ground deformation measurements. *IEEE Transactions on Geoscience and Remote Sensing*, 45(6), 1529–1558. https://doi.org/10.1109/TGRS.2006.888937

Li, H., Van Der Woerd, J., Sun, Z., Si, J., Tapponnier, P., Pan, J., *et al*. (2012) Co-seismic and cumulative offsets of the recent earthquakes along the Karakax left-lateral strike-slip fault in western Tibet. *Gondwana Research*, 21(1), 64–87. https://doi.org/10.1016/j.gr.2011.07.025

Li, H., Pan, J., Lin, A., Sun, Z., Liu, D., Zhang, J., *et al*. (2016) Coseismic surface ruptures associated with the 2014 M_w 6.9 Yutian earthquake on the Altyn Tagh Fault, Tibetan Plateau. *Bulletin of the Seismological Society of America*, 106(2), 595–608. https://doi.org/10.1785/0120150136

Li, X., Li, C., Wesnousky, S.G., Zhang, P., Zheng, W., Pierce, I.K.D. & Wang, X. (2017) Paleoseismology and slip rate of the western Tianjingshan fault of NE Tibet, China. *Journal of Asian Earth Sciences*, 146, 304–316. https://doi.org/10.1016/j.jseaes.2017.04.031

Lienkaemper, J.J. & Strum, T.A. (1989) Reconstruction of a channel offset in 1857(?) by the San Andreas fault near Cholame, California. *Bulletin of the Seismological Society of America*, 79(3), 901–909. https://doi.org/10.1785/BSSA0790030901

Lin, A., Rao, G., Jia, D., Xiaojun, W., Yan, B. & Ren, Z. (2011) Co-seismic strike-slip surface rupture and displacement produced by the 2010 M_w 6.9 Yushu earthquake, China, and implications for Tibetan tectonics. *Journal of Geodynamics*, 52, 249–259. https://doi.org/10.1016/j.jog.2011.01.001

Lin, Z., Liu-Zeng, J., Weldon, R.J., Tian, J., Ding, C. & Du, Y. (2020) Modeling repeated coseismic slip to identify and characterize individual earthquakes from geomorphic offsets on strike-slip faults. *Earth and Planetary Science Letters*, 545, 116313. https://doi.org/10.1016/j.epsl.2020.116313

Lindvall, S.C., Rockwell, T.K. & Hudnut, K.W. (1989) Evidence of prehistoric earthquakes on the Superstition Hills fault from offset geomorphic features. *Bulletin of the Seismological Society of America*, 79(2), 342–361. https://doi.org/10.1785/BSSA0790020342

Ma, S. & Andrews, D.J. (2010) Inelastic off-fault response and three-dimensional dynamics of earthquake rupture on a strike-slip fault. *Journal of Geophysical Research*, 115(B4), 1–16. https://doi.org/10.1029/2009jb006382

Manighetti, I., Perrin, C., Dominguez, S., Garambois, S., Gaudemer, Y., Malavieille, J., *et al*. (2015a) Recovering paleoearthquake slip record in a highly dynamic alluvial and tectonic region (Hope Fault, New Zealand) from airborne LiDAR. *Journal of Geophysical Research: Solid Earth*, 120(6), 3782–3803. https://doi.org/10.1002/2014JB011787

Manighetti, I., Caulet, C., De Barros, L., Perrin, C., Cappa, F. & Gaudemer, Y. (2015b) Generic along-strike segmentation of Afar normal faults, East Africa: Implications on fault growth and stress heterogeneity on seismogenic fault planes. *Geochemistry, Geophysics, Geosystems*, 16, 443–467. https://doi.org/10.1002/2014GC005684.Key

Manighetti, I., Perrin, C., Gaudemer, Y., Dominguez, S., Stewart, N., Malavieille, J. & Garambois, S. (2020) Repeated giant earthquakes on the Wairarapa fault, New Zealand, revealed by Lidar-based paleoseismology. *Scientific Reports*, 10(1), 1–11. https://doi.org/10.1038/s41598-020-59229-3

Mason, D.P.M. & Little, T.A. (2006) Refined slip distribution and moment magnitude of the 1848 Marlborough earthquake, Awatere Fault, New Zealand. *New Zealand Journal of Geology and Geophysics*, 49(3), 375–382. https://doi.org/10.1080/00288306.2006.9515174

McGill, S.F. & Rubin, C.M. (1999) Surficial slip distribution on the central Emerson fault during the June 28, 1992, Landers earthquake, California. *Journal of Geophysical Research*, 104(B3), 4811–4833. https://doi.org/10.1029/98JB01556

McGill, S.F. & Sieh, K. (1991) Surficial offsets on the central and eastern Garlock fault associated with prehistoric earthquakes. *Journal of Geophysical Research*, 96(B13), 21,597–21,621. https://doi.org/10.1029/91JB02030

Milliner, C.W.D., Dolan, J.F., Hollingsworth, J., Leprince, S., Ayoub, F. & Sammis, C.G. (2015) Quantifying near-field and off-fault deformation patterns of the 1992 M_w 7.3 Landers earthquake. *Geochemistry, Geophysics, Geosystems*, 16(5), 1577–1598. https://doi.org/10.1002/2014GC005693

Milliner, C.W.D., Dolan, J.F., Hollingsworth, J., Leprince, S. & Ayoub, F. (2016a) Comparison of coseismic near-field and off-fault surface deformation patterns of the 1992 M_w 7.3 Landers and 1999 M_w 7.1 Hector Mine earthquakes: Implications for controls on the distribution of surface strain. *Geophysical Research Letters*, 43(19), 10,115–10,124. https://doi.org/10.1002/2016GL069841

Milliner, C.W.D., Sammis, C.G., Allam, A.A., Dolan, J.F., Hollingsworth, J., Leprince, S. & Ayoub, F. (2016b) Resolving fine-scale heterogeneity of co-seismic slip and the relation to fault structure. *Scientific Reports*, 6(1), 1–9. https://doi.org/10.1038/srep27201

Nakata, T., Tsutsumi, H., Punongbayan, R.S., Rimando, R.E., Daligdig, J. & Daag, A. (1990) Surface faulting associated with the Philippine earthquake of 1990. *Journal of Geography (Chigaku Zasshi)*, 99, 95–112. https://doi.org/10.5026/jgeography.99.515

Noriega, G.R., Arrowsmith, J.R., Grant, L.B. & Young, J.J. (2006) Stream channel offset and Late Holocene slip rate of the San Andreas fault at the Van Matre Ranch site, Carrizo Plain, California. *Bulletin of the Seismological Society of America*, 96(1), 33–47. https://doi.org/10.1785/0120050094

Okada, Y. (1985) Surface deformation due to shear and tensile faults in a half-space. *Bulletin of the Seismological Society of America*, 75(4), 1135–1154. https://doi.org/10.1785/BSSA0750041135

Ou, Q., Kulikova, G., Yu, J., Elliott, A., Parsons, B. & Walker, R. (2020) Magnitude of the 1920 Haiyuan earthquake reestimated using seismological and geomorphological methods. *Journal of Geophysical Research: Solid Earth*, 125(8), e2019JB019244. https://doi.org/10.1029/2019JB019244

Petersen, M.D., Dawson, T.E., Chen, R., Cao, T., Wills, C.J., Schwartz, D. P. & Frankel, A.D. (2011) Fault displacement hazard for strike-slip faults. *Bulletin of the Seismological Society of America*, 101(2), 805–825. https://doi.org/10.1785/0120100035

Plafker, G. (1976) Tectonic aspects of the Guatemala Earthquake of 4 February 1976. *Science*, 193(4259), 1201–1208. https://doi.org/10.1126/science.193.4259.1201

Ponti, D.J., Rosa, C.M. & Blair, J.L. (2019) The M_w 6.0 South Napa earthquake of August 24, 2014 – observations of surface faulting and ground deformation, with recommendations for improving post-earthquake field investigations: Open-File Report, p. 64, https://pubs.er.usgs.gov/publication/ofr20191018%0Ahttp://pubs.er.usgs.gov/publication/ofr20191018

Quigley, M., Van Dissen, R., Litchfield, N., Villamor, P., Duffy, B., Barrell, D., *et al*. (2012) Surface rupture during the 2010 M_w 7.1 Darfield (Canterbury) earthquake: Implications for fault rupture dynamics and seismic-hazard analysis. *Geology*, 40, 55–58. https://doi.org/10.1130/G32528.1

Reitman, N.G., Mueller, K.J., Tucker, G.E., Gold, R.D., Briggs, R.W. & Barnhart, K.R. (2019a) Numerical model code and input files to run landscape evolution models with strike-slip faulting and measure channel offsets.

Reitman, N.G., Mueller, K.J., Tucker, G.E., Gold, R.D., Briggs, R.W. & Barnhart, K.R. (2019b) Offset channels may not accurately record strike-slip fault displacement: Evidence from landscape evolution models. *Journal of Geophysical Research: Solid Earth*, 124(12), 13,427–13,451. https://doi.org/10.1029/2019JB018596

Ren, Z., Zhang, Z., Chen, T., Yan, S., Yin, J., Zhang, P. & Zheng, W. (2016) Clustering of offsets on the Haiyuan fault and their relationship to paleoearthquakes. *Geological Society of America Bulletin*, 128, 3–18. https://doi.org/10.1130/B31155.1

Rizza, M., Ritz, J.F., Braucher, R., Vassallo, R., Prentice, C., Mahan, S., *et al*. (2011) Slip rate and slip magnitudes of past earthquakes along the Bogd left-lateral strike-slip fault (Mongolia). *Geophysical Journal International*, 186(3), 897–927. https://doi.org/10.1111/j.1365-246X.2011.05075.x

Robinson, D.P., Brough, C. & Das, S. (2006) The M_w 7.8, 2001 Kunlunshan earthquake: Extreme rupture speed variability and effect of fault geometry. *Journal of Geophysical Research: Solid Earth*, 111(B8), 1–10. https://doi.org/10.1029/2005JB004137

Rockwell, T.K. & Klinger, Y. (2013) Surface rupture and slip distribution of the 1940 Imperial Valley earthquake, Imperial Fault, southern California: Implications for rupture segmentation and dynamics. *Bulletin of the Seismological Society of America*, 103(2A), 629–640. https://doi.org/10.1785/0120120192

Rockwell, T.K., Lindvall, S., Dawson, T., Langridge, R., Lettis, W. & Klinger, Y. (2002) Lateral offsets on surveyed cultural features resulting from the 1999 Izmit and Duzce earthquakes, Turkey. *Bulletin of the Seismological Society of America*, 92(1), 79–94. https://doi.org/10.1785/0120000809

Rosu, A.M., Pierrot-Deseilligny, M., Delorme, A., Binet, R. & Klinger, Y. (2015) Measurement of ground displacement from optical satellite image correlation using the free open-source software MicMac. *ISPRS Journal of Photogrammetry and Remote Sensing*, 100, 48–59. https://doi.org/10.1016/j.isprsjprs.2014.03.002

Salisbury, J.B., Rockwell, T.K., Middleton, T.J. & Hudnut, K.W. (2012) LiDAR and field observations of slip distribution for the most recent surface ruptures along the central San Jacinto fault. *Bulletin of the Seismological Society of America*, 102(2), 598–619. https://doi.org/10.1785/0120110068

Salisbury, J.B., Haddad, D.E., Rockwell, T.K., Arrowsmith, J.R., Madugo, C., Zielke, O. & Scharer, K. (2015) Validation of meter-scale surface faulting offset measurements from high-resolution topographic data. *Geosphere*, 11, GES01197.1. https://doi.org/10.1130/GES01197.1

Salisbury, J.B., Arrowsmith, J.R., Brown, N., Rockwell, T., Akciz, S. & Ludwig, L.G. (2018) The age and origin of small offsets at Van Matre Ranch along the San Andreas fault in the Carrizo Plain, California. *Bulletin of the Seismological Society of America*, 108(2), 639–653. https://doi.org/10.1785/0120170162

Scharer, K.M., Salisbury, J.B., Arrowsmith, J.R. & Rockwell, T.K. (2014) Southern San Andreas Fault evaluation field activity: Approaches to measuring small geomorphic offsets -- challenges and recommendations for active fault studies. *Seismological Research Letters*, 85(1), 68–76. https://doi.org/10.1785/0220130108

Scott, C., Champenois, J., Klinger, Y., Nissen, E., Maruyama, T., Chiba, T. & Arrowsmith, R. (2019) The 2016 M7 Kumamoto, Japan, earthquake slip field derived from a joint inversion of differential LiDAR topography, optical correlation, and InSAR surface displacements. *Geophysical Research Letters*, 46(12), 6341–6351. https://doi.org/10.1029/2019GL082202

Sharp, R., Lienkaemper, J.J., Bonilla, M.G., Burke, D.B., Fox, B.F., Herd, D.G., *et al*. (1982) Surface faulting in the Central Imperial Valley: In the Imperial Valley, California earthquake of October 15, 1979. In: Ziony, J.I. (Ed.) *Evaluating Earthquake Hazards in the Los Angeles Region – An Earth Science Perspective. U.S.* Reston, VA: Geological Survey, pp. 119–143.

Shirahama, Y., Yoshimi, M., Awata, Y., Maruyama, T., Azuma, T., Miyashita, Y., *et al*. (2016) Characteristics of the surface ruptures associated with the 2016 Kumamoto earthquake sequence, central Kyushu, Japan. *Earth, Planets and Space*, 68(1), 1–12. https://doi.org/10.1186/s40623-016-0559-1

Sieh, K., Jones, L., Hauksson, E., Hudnut, K., Eberhart-Phillips, D., Heaton, T., *et al*. (1993) Near-field investigations of the Landers earthquake sequence, April to July 1992. *Science*, 260(5105), 171–176. https://doi.org/10.1126/science.260.5105.171

Sims, J.D. (1994). Stream channel offset and abandonment and a 200-year average recurrence interval of earthquakes on the San Andreas fault at Phelan Creeks, Carrizo Plain, California. In *Proceedings of the workshop on Paleoseismology*, 18–22 September, U.S. Geological Survey Open-File Report 94–568, p. 170–172.

Treiman, J.A., Kendrick, K.J., Bryant, W.A., Rockwell, T.K. & McGill, S.F. (2002) Primary surface rupture associated with the M_w 7.1 16 October 1999 Hector Mine earthquake, San Bernardino County, California. *Bulletin of the Seismological Society of America*, 92(4), 1171–1191. https://doi.org/10.1785/0120000923

Tun, S.T., Wang, Y.Y., Khaing, S.N., Thant, M., Htay, N., Myo Min Htwe, Y., *et al*. (2014) Surface ruptures of the M_w 6.8 March 2011 Tarlay earthquake, Eastern Myanmar. *Bulletin of the Seismological Society of America*, 104, 2915–2932. https://doi.org/10.1785/0120130321

Wells, D.L. & Coppersmith, K.J. (1994) New empirical relationships among magnitude, rupture length, rupture width, rupture area, and surface displacement. *Bulletin of the Seismological Society of America*, 84, 974–1002. https://doi.org/10.1785/BSSA0840040974

Wesnousky, S.G. (2008) Displacement and geometrical characteristics of earthquake surface ruptures: Issues and implications for seismic-hazard analysis and the process of earthquake rupture. *Bulletin of the Seismological Society of America*, 98(4), 1609–1632. https://doi.org/10.1785/0120070111

Xiong, B. & Li, X. (2020) Offset measurements along active faults based on the structure from motion method – a case study of Gebiling in the Xorkoli section of the Altyn Tagh Fault. *Geodesy and Geodynamics*, 11(5), 1–9. https://doi.org/10.1016/j.geog.2020.05.005

Zielke, O., Arrowsmith, R.J., Ludwig, L.G. & Akçiz, S.O. (2010) Slip in the 1857 and earlier large earthquakes along the Carrizo Plain, San Andreas Fault. *Science*, 327(5969), 1119–1122. https://doi.org/10.1126/science.1182781

Zielke, O., Arrowsmith, J.R., Ludwig, L.G. & Akciz, S.O. (2012) High-resolution topography-derived offsets along the 1857 Fort Tejon earthquake rupture trace, San Andreas Fault. *Bulletin of the Seismological Society of America*, 102(3), 1135–1154. https://doi.org/10.1785/0120110230

Zielke, O., Klinger, Y. & Arrowsmith, J.R. (2015) Fault slip and earthquake recurrence along strike-slip faults – contributions of high-resolution geomorphic data. *Tectonophysics*, 638, 43–62. https://doi.org/10.1016/j.tecto.2014.11.004

Zinke, R., Hollingsworth, J. & Dolan, J.F. (2014) Surface slip and off-fault deformation patterns in the 2013 M_w 7.7 Balochistan, Pakistan earthquake: Implications for controls on the distribution of near-surface co-seismic slip. *Geochemistry, Geophysics, Geosystems*, 15(12), 5034–5050. https://doi.org/10.1002/2014GC005538

Zinke, R., Hollingsworth, J., Dolan, J.F. & Van Dissen, R. (2019) Three-dimensional surface deformation in the 2016 M_w 7.8 Kaikōura, New Zealand, earthquake from optical image correlation: Implications for strain localization and long-term evolution of the Pacific-Australian Plate Boundary. *Geochemistry, Geophysics, Geosystems*, 20(3), 1609–1628. https://doi.org/10.1029/2018GC007951

Sharp, R.V., Budding, K.E., Boatwright, J., Ader, M.J., Bonilla, M.G., Clark, M.M., *et al*. (1989) Surface faulting along the Superstition Hills fault zone and nearby faults associated with the earthquakes of 24 November 1987. *Bulletin of the Seismological Society of America*, 79(2), 252–281. https://doi.org/10.1785/BSSA0790020252

Jianbang, S, Xianyue, S & Shumo, G International Symposium on Continental Seismicity and Earthquake Prediction (Seismol. Press, 1984).

Lin, A L & Lin, s J (1998) Tree Damage and Surface Displacement, The 1931 M 8.0 Fuyun Earthquake.. *The Journal of Geology*, 106(6), 751–758. https://doi.org/10.1086/516058

SUPPORTING INFORMATION

Additional supporting information may be found in the online version of the article at the publisher's website.

How to cite this article: Reitman, N.G., Mueller, K.J. & Tucker, G.E. (2022) Surface slip variability on strike-slip faults. *Earth Surface Processes and Landforms*, 47(4), 908–935. Available from: https://doi.org/10.1002/esp.5294